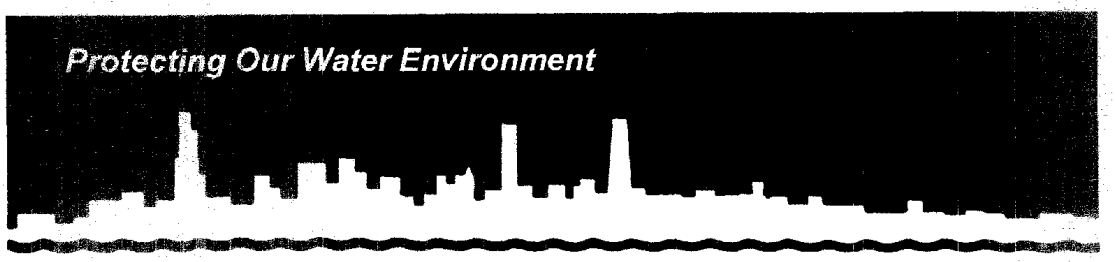

Metropolitan Water Reclamation District of Greater Chicago

RESEARCH AND DEVELOPMENT DEPARTMENT

REPORT NO. 03-13

SEDIMENTATION MANAGEMENT IN COMBINED SEWER OVERFLOW STORAGE RESERVOIRS USING WATER JETS

Progress Report

Prepared By

Ven Te Chow Hydrosystems Laboratory
Department of Civil and Environmental Engineering
University of Illinois at Urbana-Champaign

July 2003

Metropolitan Water Reclamation District of Greater Chicago
100 East Erie Street Chicago, IL 60611-2803 (312) 751-5600

SEDIMENTATION MANAGEMENT IN COMBINED SEWER OVERFLOW STORAGE RESERVOIRS USING WATER JETS

Progress Report

Prepared By

Ven Te Chow Hydrosystems Laboratory
Department of Civil and Environmental Engineering
University of Illinois at Urbana-Champaign

June 2003

Research and Development Department
Richard Lanyon, Director

July 2003

SEDIMENTATION MANAGEMENT IN COMBINED SEWER OVERFLOW STORAGE RESERVOIRS USING WATER JETS

PROGRESS REPORT

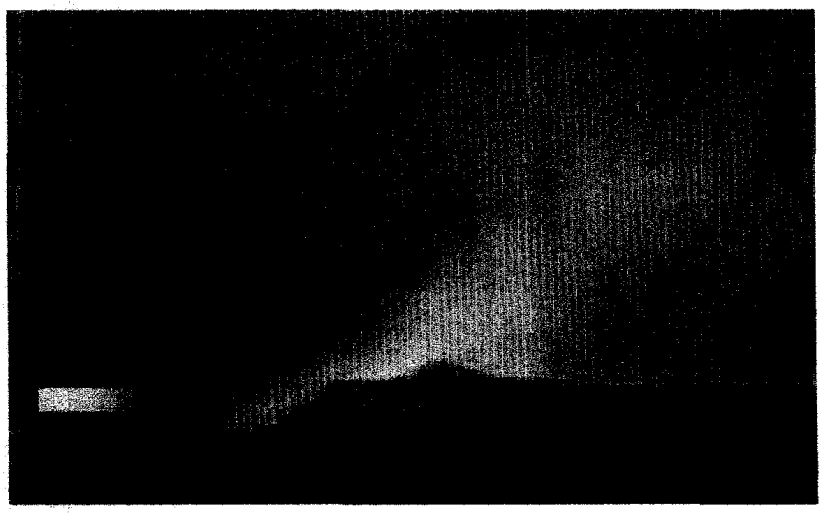

Prepared by:

Marcelo García and Yarko Niño, Principal Investigators
Jorge Abad, Mariano Cantero, Arturo León, Silvina Mangini, and Octavio Sequeiros, Research Assistants

VEN TE CHOW HYDROSYSTEMS LABORATORY
DEPARTMENT OF CIVIL AND ENVIRONMENTAL ENGINEERING
University of Illinois at Urbana-Champaign

Sponsored by:

Metropolitan Water Reclamation District of Greater Chicago

June 2003

ACKNOWLEDGMENTS

The research reported herein was done under a contract from The Metropolitan Water Reclamation District of Greater Chicago, MWRDGC, with funding provided by the U.S. Army Corps of Engineers.

TABLE OF CONTENTS

BACKGROUND

The proposed McCook Reservoir will store combined sewer overflows (CSOs) from the District's Tunnel and Reservoir Plan (TARP) system until they can be pumped back to the Stickney Water Reclamation Plant (WRP) for treatment. The McCook Reservoir will have an approximate storage capacity of 7.0 billion gallons equally divided between two stages. The stages are separated by a weir structure. A relatively small inlet stage is also part of the design. The total floor area of the reservoir is approximately 80 acres, and the maximum liquid depth will be approximately 250 feet. Based upon various assumptions regarding the suspended solids content of the CSOs and the operation of the McCook Reservoir, it is estimated that anywhere from 2100 to 6000 dry tons of solids could accumulate in the reservoir after a large storm event or a series of smaller storm events. These solids could form a layer on the reservoir floor that has been estimated by various methods as varying from 3 to 18 inches deep and having a water content somewhere between 90 and 98 percent.

The initial design plan for the McCook Reservoir is based on a horizontal reservoir floor with mechanical cleaning using street sweepers, plows, or similar vehicles to move the collected sediment to a sump for pumping back to the Stickney WRP after the reservoir has been completely dewatered. However, concerns have been raised that this will not be a cost-effective solution to the sediment handling problem, and that it may also result in odor problems in the vicinity of the reservoir due to the decomposition of the exposed solids.

It has been proposed that other methods of sediment transport/management may be feasible for McCook Reservoir. One such method is the use of water jets, in conjunction with a sloped reservoir bottom, to move the sediments to a collection sump while some volume of CSOs still remain in the reservoir to act as a liquid odor cap. The jets might be activated in conjunction with pump-back of the main liquid volume, or operated in some independent manner. The water source for the jets could be river water, if available, or the stored liquid in the reservoir. This method of sediment management has the potential to reduce the manpower costs for reservoir cleaning and also to alleviate potential odor problems. This technology may also be applicable to the Thornton Reservoir.

The Metropolitan Water Reclamation District of Greater Chicago commissioned the Hydrosystems Laboratory of the University of Illinois at Urbana-Champaign to conduct research aimed at determining whether water jets would be feasible for this application, and if such technology is feasible, developing basic design concepts for their use.

This report summarizes preliminary results obtained as part of the ongoing research project for MWRD, including a conceptualization of the problem, the research plan, and preliminary results of the experimental and numerical modeling studies conducted so far.

CONCEPTUALIZATION OF THE PROBLEM

Flow Configurations

The application of water jets for sedimentation management rests on the ability of the jetting system to resuspend bottom sediments and to create enough of a density difference with respect to the water in the reservoir so that a density current will develop along a sloping bottom, carrying the solids towards a drainage channel. This process is illustrated in Fig. 1.

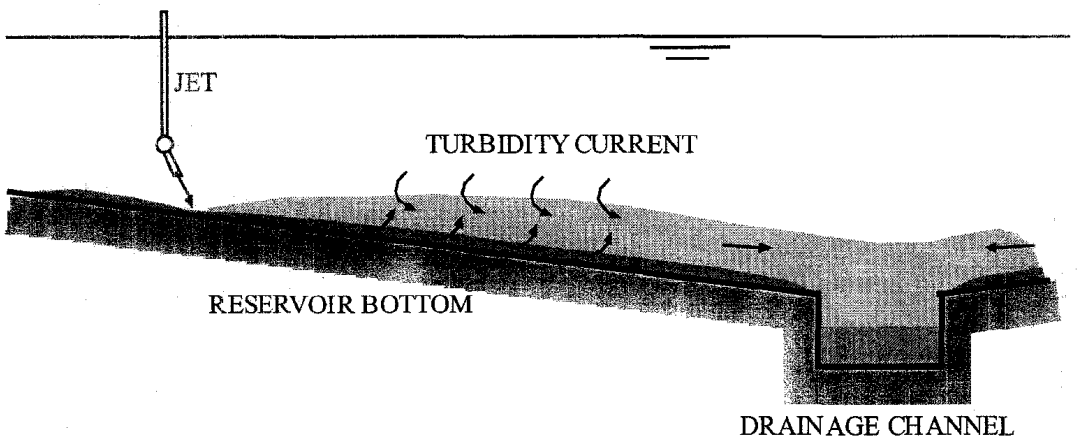

Fig. 1 Water jet induces entrainment of sediment deposited on the reservoir bottom. Buoyancy effects create turbidity current that transports suspended sediment towards drainage channel.

Various arrays of multiple jets might be needed to mobilize the sediment deposited on the bottom of the reservoir. At least, two possible array configurations are considered herein, which will probably have to be combined for the final design of the system: a) parallel jets and b) longitudinal sequence of jets (Figs. 2 and 3). The first configuration provides spatial coverage to generate uniform sediment resuspension along the reservoir (parallel to the drainage channel). The second configuration provides a sustained entraining flow in the direction perpendicular to the drainage channel, in case self-accelerating turbidity currents conditions are not met within the reservoir. Self-accelerating currents are those driven purely by buoyancy effects and able to entrain sediment into suspension, generating a feedback mechanism that increases buoyancy and erosion capacity of the flow down the slope (Parker et al., 1986).

Each of the individual jets in any of the arrays described in Figs. 2 and 3 corresponds to what is known as a wall jet, i.e., the flow is affected by the no-slip and no-penetration conditions imposed by the bottom wall of the reservoir. Besides that, since the bottom shear stress generated by the jets are supposed to entrain sediment into suspension, buoyancy effects tend to increase the initial momentum of the jet and far away from the source the flow conditions are not longer governed solely by the initial injection of fluid,

but a sediment balance, leading to erosion or deposition along the sloping bottom, and ambient water entrainment into the density current, ultimately determine its fate. Taking this behavior into account, it is convenient to define near- and far-field regions to analyze the flow in the vicinity of the jet discharge, or further away down the slope, once buoyancy forces and sediment transport processes take over as the driving mechanisms of the current, respectively.

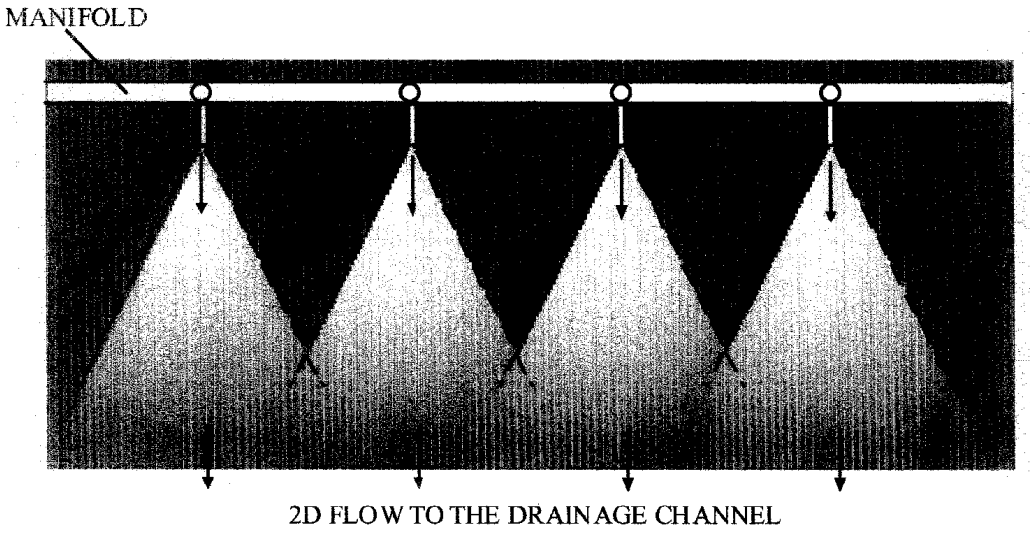

Fig. 2 Array of parallel jets. Plan view. Jet interaction creates 2D density current moving along sloping bottom towards drainage channel.

The near field of an isolated jet comprises the region where the jet flow gets established as it is discharged into the ambient fluid. It includes the developing wall boundary layer and the expansion of the flow into the ambient fluid associated with the entrainment of ambient water, which causes a downslope decay of flow velocity and wall shear stress (Rajaratnam, 1976). Despite the decay of wall shear stress, erosion and entrainment into suspension of sediment deposited on the bed occurs as long as the bottom shear stress exceeds threshold or critical values (Hogg et al., 1997).

The far field of an isolated jet discharge is the region where buoyancy effects, generated by the sediment originally suspended in the near field, constitute the main driving force of the flow and the velocity and shear stress induced by the initial wall jet are mostly dissipated. Hence, the far field of a jet discharge corresponds to the region where a turbidity current develops along the sloping bed of the reservoir. The fate of such current (self-acceleration or extinction further downslope) depends on the ability of the buoyancy induced flow field to generate sediment entrainment rates in excess of deposition rates.

A further distinction is required in the case of parallel jets, when several jets of an array configuration such as that of Fig. 2 are operated simultaneously. Due to the lateral expansion of the jets, the flow fields generated by them eventually come to interact, as

illustrated in Fig. 2. At a certain distance from the sources, which depends on the spacing between jets (the pitch, s), the initially 3D flow associated with each individual jet becomes 2D, that is, uniform in the transverse (along the reservoir) direction. According to Wang et al. (2001) such distance, L_{2D}, is about 12 s. Thus in the case of parallel jets, the near- and far-field distinctions and the behavior of the flow in each region depend on how L_{2D} compares with the distance from the jet discharge at which the resulting turbidity current becomes fully established, L_t. Cantero (2002) did numerical simulations of turbidity currents generated by a plane jet discharging tangential to a sediment bed. An analysis of those simulations suggests that L_t is of the order of 100 times the thickness of the initial jet. Therefore, the characteristics of the flow in the near- and far-field regions depend on the design parameters of the jet system (pitch, size of the nozzles). A reasonable assumption, however, is to consider that the pitch will be large enough so $L_{2D} > L_t$, and the turbidity currents generated by individual jets will become fully established before interacting with flow fields generated by neighboring jets. In such case, it is convenient to define a near field identical to that of an isolated jet discharge, an intermediate field, comparable to the far field of an isolated jet discharge, and a far field consisting of a 2D turbidity current (uniform in the transverse direction) generated by the interacting currents of the parallel jet system.

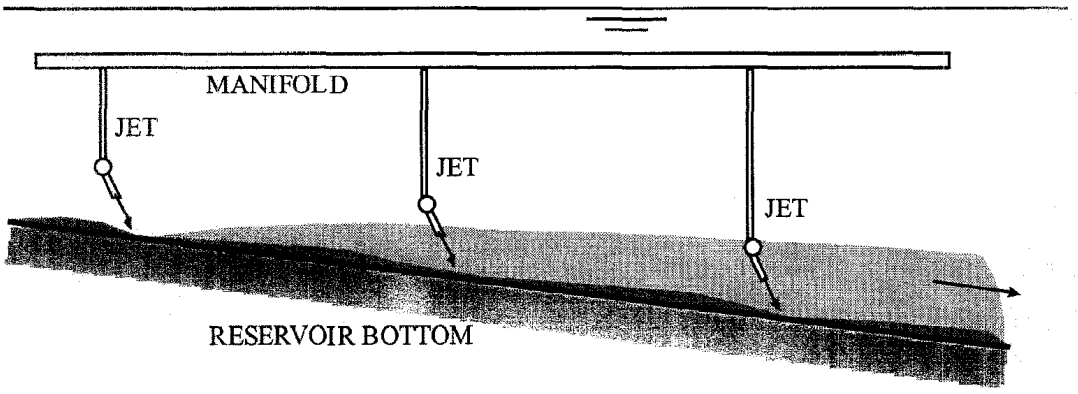

Fig. 3 Longitudinal sequence of jets (side view). In case the turbidity currents are not self-accelerating, the sequence of jets induces entrainment of sediment into suspension along the bottom and the turbidity currents provide the downslope transport.

In the case of a longitudinal sequence of jets (Fig. 3), it is assumed that the spacing of the jets will be greater that L_t, and possible comparable to L_{2D}. This suggests that the behavior of the downstream jets will be influenced by the presence of a near 2D turbidity current. Thus, the transition from the 3D near field to the 2D far field in the case of the downstream jets would be swifter than in the case of the jet at the upstream end of the sequence and the definition of an intermediate field in this case would not be justified.

Scouring and Sediment Transport Processes

i) Near field

Jenkins et al. (1981) and Dellaripa and Bailard (1986) have studied the use of jet arrays to manage sedimentation problems at Navy port facilities. The typical array configuration used, with 10 to 25 jet nozzles with a pitch of about 3 to 7 m and nozzle diameters of about 2 to 7 cm, cover spans of about 50 to 100 m with scour radius of about 15 to 30 m (Fig. 4). The scour radius is defined as the distance away from the jet, in the streamwise direction, that is scoured by the action of the induced flow field. The concept is that the bottom shear stress induced by a jet decays away from the source, therefore entrainment and scouring of bottom sediments will prevail only as long as the bottom shear stress exceeds the threshold scour stress of the sediment (Jenkins et al., 1981). The jet array is operated sequentially in time, using either one or several jet nozzles simultaneously at a time. Jenkins et al. used a 150 hp centrifugal pump, with a total discharge of about 120 l/s.

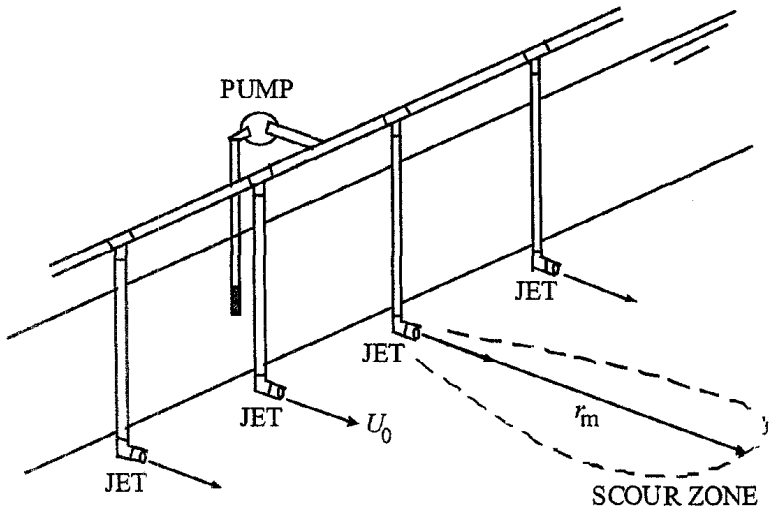

Fig. 4 Jet array system used by Jenkins et al. (1981); r_m represents the scour radius.

A similar system might be used in McCook reservoir to provide the near field conditions for turbidity currents to develop, which would carry the suspended sediment down the slope and into the drainage channel. A network of jet arrays such as those of Fig. 4 would provide spatial coverage to maintain the reservoir free of sediment deposits. The network would be operated sequentially in time to optimize the cost of the cleaning process.

Consider an individual jet nozzle with a diameter d, located at a height h over the sediment bed, under a water column of total height H, having a discharge velocity U_0 at an angle θ with respect to the horizontal (Fig. 5). No density difference is assumed between the fluid discharged by the jet and the ambient fluid.

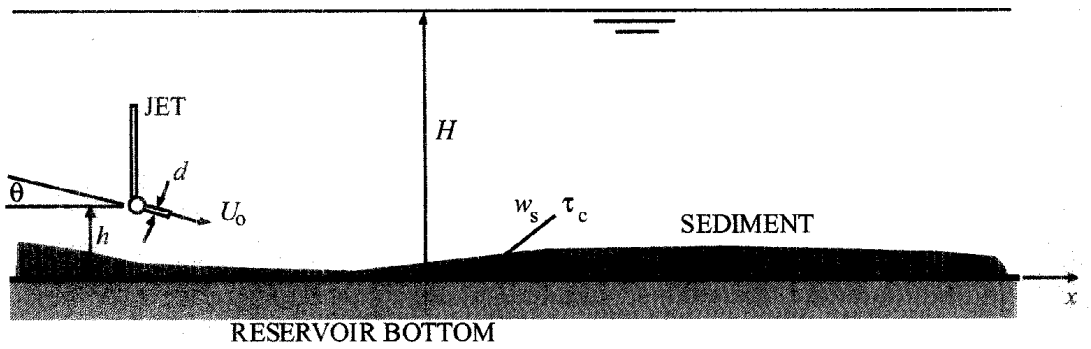

Fig. 5 Circular jet impinging over sediment bed.

The shear stress exerted by a jet on a bottom surface, τ_b, is given by an expression such as:

$$\tau_b = f_1(U_0, d, h, \theta, H, \nu, \rho, x, y) \quad (1)$$

where ν and ρ denote kinematic viscosity and density of the jet fluid, respectively, and x and y denote longitudinal and transverse coordinates, respectively. Note that no dependence on gravity has been included, as there are no buoyancy effects involved and the flow is driven by inertia balanced by bottom friction. In dimensionless terms, equation (1) reduces to:

$$\tau_b / (\rho\ U_0^2) = \phi_1(h/d, H/d, \theta, Re_0, x/d, y/d) \quad (2)$$

where $Re_0 = U_0\ d/\nu$ denotes the jet Reynolds number. In the case of a deep reservoir, the dependence on H/d can be neglected as this parameter approaches infinity. Dellaripa and Bailard (1986) suggest that the scouring area is maximized with $h = 0$ and an angle θ of about 10 degrees, although in the latter case the improvement is only mild with respect to the case when $\theta = 0$. For $h = 0$, $\theta = 0$ and large H/d, Jenkins et al. (1981) proposed the following relationship for the decay of the bottom shear stress along the x axis, which completely agrees with the present dimensional analysis:

$$\tau_b / (\rho\ U_0^2) = 120\ Re_0^{-0.4}\ (x/d)^{-2.4} \quad (3)$$

The jet Reynolds number appears to be the dominant parameter that determines the bottom shear stress even in fully developed turbulent jets. In Appendix A, a theoretical analysis of the bottom shear stress induced by a wall jet, which supports the results obtained from this dimensional analysis, is presented. On the other hand, Wygnanski et al. (1992) suggest that the dependence on Re_0 indicated by (3) disappears for values of this parameter larger than about 10^4.

According to Jenkins et al. (1981) the design of a jet for sediment management purposes can be done with the help of (3) by setting U_0 and d in order to have, at a nominal distance $x = r_m$ (the scouring radius), a bottom shear stress, τ_b, that exceeds the threshold or critical stress for the scour of the bottom sediments, τ_c. This can be analyzed as follows.

Consider a threshold shear velocity, u_{*c}, such that $\tau_c = \rho\, u_{*c}^2$, the scouring radius is then given by a relationship such as:

$$r_m = f_2(U_0, d, h, \theta, H, \nu, u_{*c}) \tag{4}$$

which in dimensionless terms can be written as:

$$r_m/d = \phi_2(h/d, H/d, \theta, Re_0, U_0/u_{*c}) \tag{5}$$

Similarly the lateral extension of the area scoured by the jet, y_m, is given by

$$y_m/d = \phi_3(h/d, H/d, \theta, Re_0, U_0/u_{*c}) \tag{6}$$

The dimensions of the scour pattern have been studied experimentally by Van Dorn et al. (1978). Dellaripa and Bailard (1986) argue, based on the data of Van Dorn et al., that the scouring area of the jet is self-similar such that the ratio y_m / r_m remains constant, taking a value of about 1/3.

Boundary conditions needed for the analysis of the far field behavior of the flow, or region where the subsequent turbidity current develops, corresponds to the relative density difference of the current at the onset, $\Delta\rho/\rho$, where $\Delta\rho = \rho_m - \rho$, and ρ_m denotes the density of the sediment-water mixture, and the corresponding mass flow rate per unit width, g_s. These variables are given by the following expressions:

$$\Delta\rho/\rho = f_3(U_0, d, h, \theta, \nu, w_s, u_{*c}, x, y) \tag{7}$$

$$g_s = f_4(U_0, d, h, \theta, \nu, \rho, w_s, u_{*c}, x, y) \tag{8}$$

where the settling velocity of the sediment particles, w_s, has been added as one of the independent variables, characterizing the suspension characteristics of the sediment. The fall velocity takes into account parameters such as sediment size, shape and density, cohesiveness and gravity effects, etc. In these relationships the total depth of the reservoir, H, has been taken out of the analysis assuming H/d is very large. Corresponding dimensionless relations are:

$$\Delta\rho/\rho = \phi_4(h/d, \theta, Re_0, U_0/w_s, U_0/u_{*c}, x/d, y/d) \tag{9}$$

$$g_s/(\rho\ U_0\ d) = \phi_5(h/d, \theta, Re_0, U_0/w_s, U_0/u_{*c}, x/d, y/d) \quad (10)$$

Note that the effect of gravity is included through the settling velocity. The erosion capacity of the jet-induced flow is dominated by inertia and friction. This changes in the far field, where buoyancy is the main driving force of the subsequent turbidity current.

ii) Far field

The far field is the region where the turbidity current generated by the jet-induced sediment suspension develops, carrying the suspended sediment down the slope towards the drainage channel of the reservoir. The main variable of this process corresponds to the mass transport rate of the turbidity current, g_s, as it determines the ultimate cleaning efficiency of the jet system. The following expression can be considered:

$$g_s = f_5(U_0, d, h, \theta, \nu, \rho, g', w_s, u_{*c}, x, y) \quad (11)$$

where $g' = g\ \Delta\rho/\rho$, with g denoting gravitational acceleration, is the reduced gravity at the onset of the current which represents the main driving force of the flow in the far field. The resulting dimensionless relation is:

$$g_s/(\rho\ U_0\ d) = \phi_6(h/d, \theta, Re_0, Fr_{d0}, U_0/w_s, U_0/u_{*c}, x/d, y/d) \quad (12)$$

where Fr_{d0} denotes the densimetric Froude number defined as $Fr_{d0}^2 = U_0^2/(g'\ d)$. In equation (12) the parameter U_0/w_s controls the characteristics of the sediment suspension, such as concentration distribution and deposition rate, while the parameter U_0/u_{*c} controls the erosive capacity of the turbidity current.

Instead of using the jet parameters in the relationship for g_s the velocity and height of the flow at the onset of the current, U_i and h_i, respectively, can be used to obtain:

$$g_s/(\rho\ U_i\ h_i) = \phi_7(Ri_i, U_i/w_s, U_i/u_{*c}, x/d, y/d) \quad (13)$$

where $Ri_i = g'\ h_i/U_i^2$ is the Richardson number at the onset of the current, which has been used instead of the densimetric Froude number of the flow (which is just the inverse of Ri_i) to be consistent with classical analyses of density currents (e.g., Ellison and Turner, 1959). In this relation the dependence on the kinematic viscosity was neglected, assuming fully developed turbulent flow (Ellison and Turner, 1959). Again, U_i/w_s controls the concentration distribution and deposition rate, while U_i/u_{*c} controls the erosive capacity of the turbidity current.

A model of flow and sediment transport by turbidity currents based on a two-phase flow analysis (Cantero, 2002) is presented in Appendix B. This mathematical model provides the basis for a numerical model that has been developed to simulate 2D turbidity currents in McCook reservoir under different initial flow conditions and sediment properties.

The design of the jet system in McCook reservoir must provide the conditions for which g_s remains relatively constant or increases with x in the far field region of the flow. This ensures that the sediment scoured by the jets in the near field is evacuated from the system and, eventually, that the turbidity currents also contribute to eroding the sediment deposit to some extent.

Research Needs

From the analyses of previous sections it is concluded that a number of different flow situations and sediment characteristics must be studied in order to understand the phenomena involved and gather sufficient knowledge to design the sediment management system of McCook reservoir using water jets. These are:

1. Flow and sediment transport processes

- Flow and scour pattern of a jet impinging on a sediment deposit of limited thickness
- Flow field and bottom shear stress generated by parallel wall jets
- 2D eroding/depositing turbidity current
- 3D laterally expanding eroding/depositing turbidity current
- Interaction of jet and 2D turbidity current

2. Characterization of McCook sediments

- Settling velocity
- Critical shear stress for erosion
- Suspension dynamics

Although the information provided by Jenkins et al. (1981) and Dellaripa and Bailard (1986) regarding the design of jet array systems to manage sediment deposits in port facilities is useful for the McCook study, there are some aspects of such application that are different to the present one. In particular, the sediment deposit in McCook reservoir is going to be of a limited thickness (estimated by MWRD as about 0.1 to 0.5 m), which means that the scouring process will be limited by the solid bottom of the reservoir, changing the geometry of the scour zone and the scour radius in particular (Fig. 4), with respect to those given by the relationships proposed by Dellaripa and Bailard (1986).

Another aspect that needs to be investigated corresponds to the flow and sediment concentration conditions prevailing at the onset of the turbidity current, at the edge of the near field zone generated by the jet array. These constitute the boundary conditions that control the developing turbidity current in the far field zone of the jet arrays. Jenkins et al. (1993) report sediment entrainment fluxes created by jets in port facilities and propose a theory to estimate them. This information can be used to some extent to estimate sediment concentration and mass fluxes created by jet arrays at McCook reservoir, however its application to the latter conditions is not direct, particularly because of the

limited thickness of the sediment deposit and the presence of the solid bottom of the reservoir.

To address the lack of knowledge needed for the design of the jetting sediment management system in McCook reservoir, different series of experiments are being conducted, with the aim of establishing flow and sediment transport conditions within the near field zone and to, some extent, the beginning of the far field zone.

As concluded from the analysis of the previous section, the near field sediment transport problem depends, among other dimensionless parameters, on Re_0, U_0/w_s, and U_0/u_{*c}. A consequence of this result is that the only way to physically model the field situation meaningfully, i.e., without introducing major scale distortions, is by reproducing both the Reynolds number and the sediment of the prototype, and this results in the need to use a 1:1 model scale which is unpractical. Even though it can be argued that Re_0 would not be a relevant parameter in the prototype and therefore it may not necessarily be reproduced exactly in the laboratory experiments as long as it is large enough in those experiments, the need to reproduce the response of the sediment, which in McCook case it seems to be a complicated one given the origin of those sediments, imposes the use of prototype sediments in the experimental study and this leads, by dimensional considerations, to the need to reproduce also prototype flow velocities in the experiments.

The response of the sediments has been characterized in the previous section by essentially two parameters: the settling velocity, w_s, and the threshold or critical scour stress of the bottom sediments, τ_c. It has been observed in preliminary tests with solids provided by MWRD that they behave as cohesive sediment to some degree, and therefore both w_s and τ_c will probably depend on the degree of consolidation of the deposit. One of the main objectives of the present study is, therefore, to learn about the expected behavior of McCook sediments and its effect on the jetting management system.

These topics define specific objectives for the ongoing research and the strategy used to approach their study is explained in the following section.

THE RESEARCH PLAN

Given that the experimental research on the behavior of the jetting sediment management system requires model scales close to unity, which are not possible to obtain at a laboratory scale, an alternative approach is being used in the present study. This approach consists of combining experiments and numerical modeling of flow and sediment transport induced by the jet array systems. The idea is to validate the main aspects of the numerical models at a laboratory scale, using conditions that probably differ from those expected in the prototype, and then use those numerical models for the final design of the jetting system for McCook reservoir. Based on this strategy, the following research plan is envisioned, many aspects of which are already under study. A summary of preliminary results obtained so far, are presented in the next section.

Flow and Sediment Transport Process

Experimental studies

E1 Experimental study on flow and scour pattern of isolated and parallel jets impinging on a sediment deposit of limited thickness
E2 Experimental study on the onset of turbidity current by jet impinging on a sediment deposit of limited thickness
E3 Experimental study on the interaction of jet and 2D turbidity current

Numerical studies

N1 Numerical study of flow field and bottom shear stress generated by isolated and parallel wall jets
N2 Numerical study of sediment transport process induced by isolated and parallel jets impinging on a sediment deposit of limited thickness
N3 Numerical modeling of eroding/depositing turbidity current
N4 Numerical modeling of the interaction of jet and 2D turbidity current

The experiments are being conducted in an existing water tank (7.3 m by 2.7 m horizontal area and 2.3 m height) having a plate 5.4 m long and 2.5 m wide, with adjustable slope, representing the bottom of McCook reservoir. Either a 1.7 m wide channel or a narrower partition 0.3 m wide are being used to study the behavior of circular or plane jets impinging, either parallel to or at an angle with respect to a sediment bed of a given thickness. The sediments used in the study range from a fine quartz material provided by U.S. Silica Company, with a mean size of about 19 to 45 □m, to sediments that are representative of those that will be deposited on McCook reservoir (provided by MWRD). During the experiments the flow field generated by the jet discharge is monitored by means of an array of 4 synchronized ADVs (Acoustic Doppler Velocimeter). Erosion rates are registered by means of surveys of the bed elevation and also, in some cases, through the analysis of video records of the erosion process. Sediment concentrations generated by the entrainment process are measured through samples taken from the water column.

The numerical studies are based on two different models: Flow3D, a commercial software, and a depth-averaged turbidity current model based on two-phase flow equations, developed by our research group (Cantero, 2002). Flow3D is being used to simulate the near field flow structure and bottom shear stress generated by isolated and parallel jets, while the turbidity current model is being used to simulate the far field flow and sediment transport properties of turbidity currents, including erosion and deposition processes, given a set of conditions at the onset of the current and sediment properties, such as settling velocity and entrainment rates. Values of these properties for McCook sediments are going to be determined from the characterization study explained next.

Characterization of McCook Sediments

The characterization of sediments representative of those to be deposited on the bottom of McCook reservoir is being done by means of a number of different experiments. They concentrate on the following aspects:

S1 Settling velocity
S2 Critical shear stress for erosion
S3 Suspension dynamics
S4 Near field erosion rates

The experiments S1, to characterize settling velocity, are being conducted with the help of a laser-diffraction instrument: LISST-ST. This instrument measures size distribution, concentration, and settling velocity distribution of suspended particles, among other parameters. The characterization of the settling velocity of McCook-type sediments (provided by MWRD) is being made considering dependence on both sediment concentration and aggregate formation.

The experiments S2 and S3 are being conducted in an annular flume with an inner radius of 0.55 m, an outer radius of 0.75 m, and a total depth of 0.45 m, and with a rotating upper lid and an also rotating bottom plate. The main advantage of using this type of flume for cohesive sediment research is that motion is transmitted to the fluid by means of wall friction, which prevents flocs to be broken up by pumps, thus preserving the aggregate structure of the suspended sediment during the experiments. The flow within the annular flume has, at least theoretically, a uniform shear stress distribution, which facilitates the analysis of the response of the sediment (entrainment from the bed, concentration distribution, change in the aggregate structure of the suspended sediment, etc.) to flow conditions. Measurements in experiments S2 and S3 include characterizing the flow field by means of an ADV that rotates with the upper lid of the flume, measuring concentration distribution and suspended sediment properties by analyzing samples taken from the flume, and direct observations of the behavior of the sediment suspensions.

The experiments S4 are to be conducted in the water tank of experiments E1. By tracking the time evolution of a sediment bed formed with McCook-type sediments, in response to the scour generated by a plane wall jet, an estimation of the erosion rate in the near field of those sediments can be obtained. Preliminary observations indicate that an erosion front is created by the impact of the jet on the sediment bed, which moves in the streamwise direction at a rate that is proportional to the erosion rate created by the jet. Video recordings will be used to estimate the velocity of the erosion front, which will provide the estimation of the near field erosion rate of the jet.

The experiments S1 to S4 will consider the effect of different degrees of consolidation of the bottom sediments in McCook reservoir, by starting from mechanically disaggregated samples and allowing them to consolidate for times ranging from 0 to a few days, which is the estimated residence time for the sediments within the reservoir.

PRELIMINARY RESULTS

Characterization of Sediments

A series of experiments have been conducted to characterize sediment properties of solids from O'Hare reservoir, provided by MWRD. A report on the results of those experiments (belonging to series S1 described in previous sections) is presented in Appendix C. The LISST-ST laser-diffraction instrument was used for the analyses. Different test samples were prepared from the solids provided by MWRD. Solid concentrations used in those samples varied between 2 and 20 ml/l. Tests with and without disaggregated samples were made in order to estimate the size of aggregate formation. The mean size of particles belonging to the original samples (not disaggregated) is about 24.5 μm, and the typical settling velocity is 0.05 cm/s, while corresponding values for disaggregated samples were 10.8 μm and 0.008 cm/s, respectively. Although more tests are needed, the results obtained so far indicate a negligible dependence of the settling velocity on sediment concentration and this applies to both the original and disaggregated samples. The mean size of the aggregates found in the original sediment samples (not disaggregated) was estimated indirectly, from particle size and concentration distributions measurements. The results indicate that the mean diameter of the aggregates is about 84 μm with a mean settling velocity of 0.5 cm/s. Given the range of particles sizes found in this preliminary study, it is concluded that this sediment can be considered as cohesive.

The results from the sediment characterization analysis suggest that the type of solids to be deposited within McCook reservoir might be characterized as to be composed mainly by two fractions: a disperse fraction and flocs or aggregates of larger size and higher settling velocity. The time scale associated with the formation of those aggregates is currently being investigated, as well as their response to turbulence and flow shear stresses. This information is important for modeling purposes as is discussed in Appendix B, where the mathematical model for the far-field flow and sediment transport by turbidity currents to be used in the present study is presented.

To study the response of the reservoir sediments to shear stress and turbulence, experiments belonging to series S2 and S3 described previously are being conducted in an annular flume. A description of the experimental facility and methods is presented in Appendix D.

Flow and Erosion in the Near Field of Jets

Two different studies are being conducting regarding flow and erosion in the near field of jets. The first one corresponds to a 3D numerical simulation of the flow field generated by isolated and parallel jets (series N1 described in previous sections). Flow3D is being used for this purpose. An example of the results obtained is shown in Appendix E, where the flow field generated by a series of 5 wall jets, with nozzle diameter d = 0.1 m and pitch s = 1 m, simultaneously discharging water into a stagnant layer of water of the same properties, tangentially to the bottom wall of the reservoir and with a velocity of 1 m/s,

are presented. These are just preliminary results of a more comprehensive study, covering different conditions such as number of jets, pitch, nozzle diameter, jet velocity, etc.

The second ongoing study regarding the near field of jets is an experimental study belonging to series E1 and E2. The experiments are being conducted in the water tank described in previous sections, within the 0.3 m wide channel partition, using a bottom slope of about 1.5%. A plane wall jet is discharged into the channel, parallel to the bottom (see Appendix F). Two different situations are being analyzed using either a fixed bottom or a movable bed formed with a fine quartz material, having a mean size of about 19 to 45 μm. The flow field in the experiments was measured with a set of four ADVs located at different positions along the channel. Video recordings were used in the experiments with sediment beds, to track the erosion generated by the jets. This methodology will also be applied to study erosion rates characteristic of McCook type of solids, for series S4. Appendix F summarizes some of the preliminary results obtained.

REFERENCES

Cantero (2002) Theoretical and numerical modeling of turbidity currents as two-phase flows. Thesis submitted in partial fulfillment of the requirements for the degree of Master of Science in Civil and Environmental Engineering. University of Illinois at Urbana-Champaign.

Dellaripa and Bailard (1986). Studies of scour patterns produced by rotating jets in a flow field. NCEL Technical Note N-1753. Naval Civil Engineering Laboratory, Port Hueneme, California.

Ellison, T.H. and Turner, J.S. (1959) Turbulent entrainment in stratified flows. *J. Fluid Mech.* 6, pp. 423-448.

Hogg, A.J., Huppert, H.E., and Dade, W.B. (1997). Erosion by planar turbulent jets. *J. Fluid Mech.* 338, pp. 317-340.

Jenkins, S.A., Aijaz, S., and Wasyl, J. (1993). Transport of fine sediments by hydrostatic jets. In Nearshore and Estuarine Cohesive Sediment Transport, ed. by A. Mehta, Coastal and Estuarine Studies, American Geophysical Union.

Jenkins, S.A., Inman, D.L., and Van Dorn, W.G. (1981). The evaluation of sediment management procedures. Phase IV-VI Final Report. SIO Reference Series No. 81-22. Scripps Institution of Oceanography.

Parker et al., (1986) Parker, G., Fukushima, Y. and Pantin, H. (1986). Self-accelerating turbidity currents". *J. Fluid Mech.* 171, pp. 145-181.

Rajaratnam, N. (1976). Developments in Water Sciences: Turbulent jets. Elsevier.

Van Dorn, W.G., Inman, D.L, and McElmury, S. (1978). Evaluation of sediment management procedures; Phase I, II, and III, Final Report. SIO Reference Series No. 7532. Scripps Institute of Oceanography.

Wang, J., Priestman, G., and Wu, D. (2001). An analytical solution for incompressible flow through parallel multiple jets. *J. Fluids Engineering*, vol. 123, pp. 407-410.

Wygnanski, I., Katz, Y., and Horev, E. (1992). On the applicability of various scaling laws to the turbulent wall jet. *J. Fluid Mech.* 234, pp. 669-690.

APPENDIX A
Plane Wall Jet

An analysis of the bottom shear stress behavior

Consider a plane jet developing along an inclined plane with slope S, intruding into a stagnant ambient fluid (Fig. 1). The initial velocity and thickness of the flow are U_0 and h_0 respectively. No density differences are considered between the discharged fluid and the ambient fluid.

1 Governing Equations

If h is a measure of the thickness of the density current and H denotes the total depth of the ambient fluid, it is assumed that $h/H << 1$. With this assumption, boundary layer approximations are invoked to simplify the equations governing the motion of the density current.

The Reynolds averaged equations for a 2D flow in the $x - z$ plane of Fig. 1 are:

$$\rho \{\frac{\partial \bar{u}}{\partial t} + \bar{u} \frac{\partial \bar{u}}{\partial x} + \bar{w} \frac{\partial \bar{u}}{\partial z}\} = -\frac{\partial \bar{p}}{\partial x} + \rho \nu \{\frac{\partial^2 \bar{u}}{\partial x^2} + \frac{\partial^2 \bar{u}}{\partial z^2}\} + g \rho S - \rho \frac{\partial \overline{u'^2}}{\partial x} - \rho \frac{\partial \overline{u'w'}}{\partial z} \quad (1)$$

$$\rho \{\frac{\partial \bar{w}}{\partial t} + \bar{u} \frac{\partial \bar{w}}{\partial x} + \bar{w} \frac{\partial \bar{w}}{\partial z}\} = -\frac{\partial \bar{p}}{\partial z} + \rho_0 \nu \{\frac{\partial^2 \bar{w}}{\partial x^2} + \frac{\partial^2 \bar{w}}{\partial z^2}\} - g \rho - \rho \frac{\partial \overline{w'^2}}{\partial z} - \rho \frac{\partial \overline{u'w'}}{\partial x} \quad (2)$$

$$\frac{\partial \bar{u}}{\partial x} + \frac{\partial \bar{w}}{\partial z} = 0 \quad (3)$$

where (1) and (2) correspond to the momentum equations in directions x and z, respectively, and (3) corresponds to the conservation of volume equation. In those equations $\bar{u}$ and $\bar{w}$ denote the streamwise and bed normal velocity components averaged over the turbulence, $\bar{p}$ denotes thermodynamic pressure averaged over the turbulence, ν denotes kinematic viscosity of the moving fluid, and the terms $\overline{u'^2}$, $\overline{w'^2}$, $\overline{u'w'}$, represent Reynolds turbulent stresses.

To reduce the Reynolds averaged equations, boundary layer approximations are introduced. For that, the following scaling is used:

$$\bar{u} \propto U \quad ; \quad z \propto h \quad ; \quad x \propto L \quad ; \quad \beta \propto B \quad (4)$$

where U denotes the maximum velocity characteristic of the wall jet, h denotes the height of the current, and L denotes a length scale in the streamwise direction. The boundary layer approximation is obtained by invoking the condition: $h/L << 1$.

To further simplify the analysis, the assumption of a steady wall jet is considered.

From (4) it is concluded that

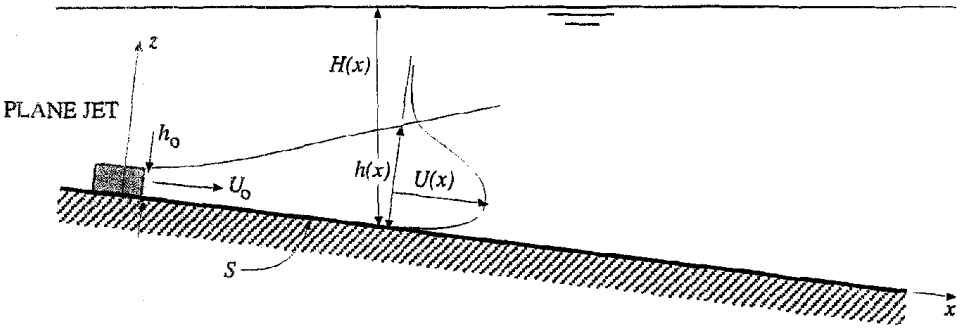

Figure 1: Plane jet along inclined bottom intruding into staganant ambient fluid.

$$\frac{U}{L} \propto \frac{W}{h} \tag{5}$$

and therefore $W \propto U\ h/L$, where W is a measure of the bed normal velocity scale. Since $h/L << 1$ then it is obvious that W is of a lower magnitude than U.

Introducing the scales U, W, h and L, neglecting the term:

$$\frac{\overline{u'^2}}{U^2} << 1 \tag{6}$$

it is possible to reduce (1) to:

$$\rho \{\bar{u} \frac{\partial \bar{u}}{\partial x} + \bar{w} \frac{\partial \bar{u}}{\partial z}\} = -\frac{\partial \bar{p}}{\partial x} + g\ \rho\ S + \rho\ \nu \frac{\partial^2 \bar{u}}{\partial z^2} - \rho \frac{\partial \overline{u'w'}}{\partial z} \tag{7}$$

or, simply expressing the total, viscous plus turbulent, longitudinal shear stress as:

$$\tau_{zx} = \rho\ \nu \frac{\partial \bar{u}}{\partial z} - \rho\ \overline{u'w'} \tag{8}$$

yields:

$$\rho \{\bar{u} \frac{\partial \bar{u}}{\partial x} + \bar{w} \frac{\partial \bar{u}}{\partial z}\} = -\frac{\partial \bar{p}}{\partial x} + g\ \rho\ S + \frac{\partial \tau_{zx}}{\partial z} \tag{9}$$

Repeating the same procedure for (2) yields the hydrostatic pressure approximation:

$$0 = -\frac{\partial \bar{p}}{\partial z} - g\ \rho \tag{10}$$

Integrating (10) in the vertical and imposing a zero value for the pressure at the free surface gives an expression for the pressure distribution of the flow gives:

$$\bar{p}(x,z) = \rho\ g \int_z^{H(x)} dz \tag{11}$$

and taking the derivative of this result with respect to x yields:

$$\frac{\partial \bar{p}}{\partial x} = \rho\ g\ S \tag{12}$$

Where the relationship:

$$\frac{\partial H}{\partial x} = S \tag{13}$$

has been used, assuming a horizontal free surface, unperturbed by the submerged current.

Replacing (12) in (9) yields:

$$\rho \left\{ \bar{u} \frac{\partial \bar{u}}{\partial x} + \bar{w} \frac{\partial \bar{u}}{\partial z} \right\} = \frac{\partial \tau_{zx}}{\partial z} \tag{14}$$

It is easy to see, using the conservation of volume equation (3) that:

$$\bar{u} \frac{\partial \bar{u}}{\partial x} + \bar{w} \frac{\partial \bar{u}}{\partial z} = \frac{\partial \bar{u}^2}{\partial x} + \frac{\partial \bar{u}\bar{w}}{\partial z} \tag{15}$$

Replacing this result in (14) gives:

$$\rho \left\{ \frac{\partial \bar{u}^2}{\partial x} + \frac{\partial \bar{u}\bar{w}}{\partial z} \right\} = \frac{\partial \tau_{zx}}{\partial z} \tag{16}$$

2 Depth-averaged Equations

Next, the simplified equations of motion are integrated in the vertical. Equation (16) can be depth-averaged to obtain:

$$\frac{\partial}{\partial x} \int_0^\infty \rho \, \bar{u}^2 \, dz = -\tau_b \tag{17}$$

where the upper limit of integration, H, has been replaced by the limit $z \rightarrow \infty$, assuming $H/h >> 1$, the no-slip, no-penetration, no surface streamwise velocity and no surface shear stress boundary conditions have been imposed: $(\bar{u}\bar{w})|_{z=0} = 0$, $(\bar{u}\bar{w})|_{z=\infty} = 0$, $\tau_{zx}|_{z=0} = \tau_b$, $\tau_{zx}|_{z=\infty} = 0$, and τ_b denotes the bottom shear stress.

Integrating now (3) yields:

$$\frac{\partial}{\partial x} \int_0^\infty \bar{u} \, dz = w_e \tag{18}$$

where the boundary conditions: $\bar{w}|_{z=0} = 0$ and $\bar{w}|_{z=\infty} = -\bar{w}_e$ have been used. Here w_e denotes the entrainment velocity or rate of entrainment of ambient fluid into the density current due to mixing effects.

Equation (17) shows that the momentum flux of the flow decreases in the streamwise direction due to friction with the bed and Equation (18) shows that the volumetric discharge increases in the streamwise direction due to entrainment of ambient fluid into the current.

To continue with the analysis it is necessary to introduce further assumptions. In particular, closure relationships for the entrainment velocity, w_e, and the bottom shear stress, τ_b are required. These are specified as:

$$w_e = e_w \, U \tag{19}$$

$$\tau_b = \rho \, c_f \, U^2 \tag{20}$$

where e_w denotes an entrainment coefficient and c_f a bottom friction coefficient. Here U denotes the maximum velocity of the current induced by the wall jet.

3 Self Similar Solution

To further simplify the equations governing the motion of the density current, a self similarity hypothesis is introduced for the vertical distribution of $\bar{u}$, which reduces its dependence on x, such that a collapse of the vertical profiles of $\bar{u}$ in one unique curve, when the variables are made dimensionless using the proper scaling, is possible.

Consider the following normalization:

$$\frac{\bar{u}}{U} = f_1(\eta) \quad ; \quad \eta = \frac{z}{h} \tag{21}$$

Replacing (19), (20) and (21) in (17) and (18) yields:

$$S_1 \frac{d(U^2\, h)}{dx} = -c_f\, U^2 \tag{22}$$

$$S_2 \frac{d(U\, h)}{dx} = e_w\, U \tag{23}$$

where S_1 and S_2 are *shape factors* defined by:

$$S_1 = \int_0^\infty f^2(\eta)\, d\eta \quad ; \quad S_2 = \int_0^\infty f(\eta)\, d\eta \tag{24}$$

Introducing now power law assumptions for U and h:

$$U = U^*\, x^p \quad ; \quad h = h^*\, x^q \tag{25}$$

where p and q are some exponents and U^* and h^* proportionality factors, and assuming that the coefficients c_f and e_w are functions of the local Reynolds number of the flow defined as: $Re = U\, h/\nu$, such that they also follow power laws of the type:

$$c_f = C_1\, Re^m \quad ; \quad e_w = C_2\, Re^n \tag{26}$$

where m and n are exponents and C_1 and C_2 coefficients of proportionality, then equations (22) and (23) can be reduced to:

$$S_1\, U^{*2}\, h^*\, (2\, p + q)\, x^{(2\, p+q-1)} = -\frac{C_1}{\nu^m}\, U^{*(2+m)}\, h^{*m}\, x^{(m\,(p+q)+2\, p)} \tag{27}$$

$$S_2\, U^*\, h^*\, (p + q)\, x^{(p+q-1)} = \frac{C_2}{\nu^n}\, U^{*(1+n)}\, h^{*n}\, x^{(n\,(p+q)+p)} \tag{28}$$

On dimensional grounds, the following relationships must hold:

$$2\, p + q - 1 = m\, (p + q) + 2\, p \tag{29}$$

$$p + q - 1 = n\, (p + q) + p \tag{30}$$

which yield the simple result: $p = -1$ and $q = 1$ and necessarily $C_2 = 0$. That is, for this result to be valid there should be no entrainment of ambient fluid into the jet-induced flow and the initial discharge must remain constant along x.

Note that in a free jet, assuming $\tau_b = 0$ and $e_w = constant$ in (22) and (23), the present analysis gives: $p = -1/2$ and $q = 1$ in agreement with well known results (Rajaratnam, 1976).

Now imposing boundary conditions for the jet volumetric discharge and momentum flux, such that:

$$\int_0^\infty \bar{u}\, dz|_{x=x_0} = q_0 = U_0\, h_0 \tag{31}$$

$$\int_0^\infty \rho\, \bar{u}^2\, dz|_{x=x_0} = m_0 = \rho\, U_0^2\, h_0 \tag{32}$$

where U_0 and h_0 denote the initial velocity and height of the jet, respectively, at a reference distance $x = x_0$.

Replacing (21), (24) and (25) in (31) and (32) yields:

$$U^* = \frac{S_2}{S_1}\, U_0\, x_0 \quad ; \quad h^* = \frac{S_1}{S_2^2}\, \frac{h_0}{x_0} \tag{33}$$

which introduced into (25) and using the result $p = -1$, $q = 1$, finally gives:

$$\frac{U}{U_0} = (\frac{S_2}{S_1})\, (\frac{x_0}{x}) \tag{34}$$

$$\frac{h}{h_0} = (\frac{S_1}{S_2^2})\, (\frac{x}{x_0}) \tag{35}$$

Note that this result, as it was already discussed, leads to a constant volumetric discharge, q (no entrainment of ambient fluid into the current):

$$q = \int_0^\infty \bar{u}\, dz = S_2\, U\, h = U_0\, h_0 = q_0 \tag{36}$$

which also yields a constant Reynolds number along the x direction:

$$Re = \frac{U\, h}{\nu} = \frac{1}{S_2}\, \frac{U_0\, h_0}{\nu} = \frac{1}{S_2}\, Re_0 \tag{37}$$

where Re_0 is the Reynolds number of the initial jet discharge.

Assuming that the reference distance x_0 is proportional to the initial height of the jet such that: $x_0 = \alpha\, h_0$, then (34) and (35) can be rewritten as:

$$\frac{U}{U_0} = K\, (\frac{h_0}{x}) \tag{38}$$

$$\frac{h}{h_0} = \frac{1}{K\, S_2}\, (\frac{x}{h_0}) \tag{39}$$

where $K = \alpha\, S_2/S_1$ is a coefficient.

From (27), the following relationship is derived:

$$S_1^2\, S_2^{m-2} = c_1\, \alpha\, Re_0^m \tag{40}$$

which shows that the shape factors S_1 and S_2, and therefore K, are functions of the Reynolds number of the jet.

4 Bottom Shear Stress

Replacing (38) and (39) in (20), an expression for the shear stress exerted by the wall jet on the bottom is obtained as:

$$\frac{\tau_b}{\rho\, U_0^2} = \alpha\, (\frac{h_0}{x})^2 \tag{41}$$

Jenkins et al. (1981) report measurements of bottom shear stress exerted by a jet parallel to a smooth wall. They indicate that although a dependence: $\tau_b \propto x^{-2}$ can be deduced from similarity considerations, in agreement with the present analysis, the experimental results suggest a different exponent. They propose the following relationship from a fit to their experimental data:

$$\frac{\tau_b}{\rho\, U_0^2} = 120\, Re_0^{-0.4}\, (\frac{h_0}{x})^{2.4} \tag{42}$$

Beyond the difference in exponents of the power law relationships (41) and (42), the latter result suggests that the parameter α is also a function of the jet Reynolds number Re_0.

These results disagree with those of Hogg et al. (1997). They propose a different scaling for U and h, which is expressed in general terms as:

$$\frac{U}{U_0} = K_1\, Re_0^{(1-2\,m)}\, (\frac{h_0}{x})^m \tag{43}$$

$$\frac{h}{h_0} = K_2\, Re_0^{2\,(n-1)}\, (\frac{x}{h_0})^n \tag{44}$$

with the values $m = 0.47$ and $n = 0.88$ fitted by Wygnanski (1992) from experimental data. This scaling leads to closures for τ_b and w_e that are totally different with respect to those used in the previous section. Indeed the following results are obtained:

$$\frac{\tau_b}{\rho\, U_0^2} = S_1\, K_1^2\, K_2\, Re_0^{2\,(1-2\,m)+2\,(n-1)}\, (2\,m-n)\, (\frac{h_0}{x})^{(2\,m-n+1)} \tag{45}$$

$$\frac{w_e}{U_0} = S_2\, K_1\, K_2\, Re_0^{(1-2\,m)+2\,(n-1)}\, (n-m)\, (\frac{h_0}{x})^{(m-n+1)} \tag{46}$$

which lead to $\tau_b \propto x^{-1.06}$, with an exponent that is about half that reported by Jenkins et al. (1981), and $w_e \propto x^{-0.59}$, which implies that the entrainment is not zero as predicted by the analysis of the previous section, but it decreases as x increases.

Further comparison with experimental data is needed to test the validity of the results obtained herein and to resolve the apparent contradiction between the experimental results of Jenkins et al. (1981) and those used by Hogg et al. (1997) that lead to a different behavior of the bottom shear stress exerted by the plane jet.

5 References

- Hogg, A.J., Huppert, H.E., and Dade, W.B. (1997). Erosion by planar turbulent jets. J. Fluid Mech. 338, pp. 317-340.
- Jenkins, S.A., Inman, D.L., and Van Dorn, W.G. (1981). The evaluation of sediment management procedures. Phase IV-VI Final Report. SIO Reference Series No. 81-22. Scripps Institution of Oceanography.
- Rajaratnam, N. (1976). Developments in Water Sciences: Turbulent jets. Elsevier.
- Wygnanski, I., Katz, Y., and Horev, E. (1992). On the applicability of various scaling laws to the turbulent wall jet. J. Fluid Mech. 234, pp. 669-690.

APPENDIX B

Mathematical model for the far field flow and sediment transport: 2D Turbidity currents

Conceptual model of flow

The flow can be separated in two different regions with different characteristics: a near field and a far field. It is assumed here that the near field is the region where single jets interact eventually producing a two-dimensional flow [1-2], and the far field region is where the flow can be considered as two-dimensional with negligible transversal variation of both the flow velocity and the suspended sediment concentration. Figure 1 illustrates this idea.

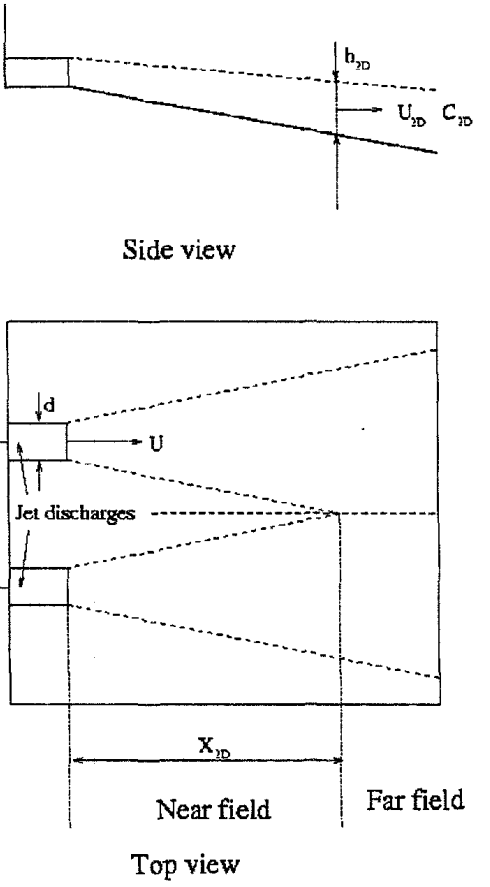

Figure 1. Conceptual model of flow. The near field is characterized by the interaction of single jets, while the far field can be considered as a 2D flow where there is no transversal variation of the flow.

In the following sections this idea and the strategy to analyze the flow in each region are explained.

Analysis of near field

In the near field the single jets interact and generate a flow that can be considered as two-dimensional. Knystautas [1] has studied experimentally the interaction of round free jets discharging from a serie of holes in lines. In his work Knystautas found that the flow can be considered quasi-two-dimensional after 12 inter-hole distances, i.e. X_{2D}=12 s. In a later analytical work about free plane jets discharging in line, Wang *et al.* [2] found that this distance varies as the third power of the pitch s. It is worth noting that both authors found that X_{2D} does not depend on the opening size of the discharge, but only on the pitch s.

The near field analysis will describe the initial conditions for the far field model. These initial conditions are shown as U_{2D}, h_{2D} and C_{2D} in Figure 1. In order to implement this idea U_{2D}, h_{2D} and C_{2D} must be determined as functions of the diameter of the jets, the initial velocity of the jets, the separation between discharges.

The strategy of this analysis in being developed at the time that this report is being written.

Analysis of far field

The far field region is characterized by the two-dimensionality of the flow. Figure 2 shows the conceptual model used in the far field for the flow. Therein a two-dimensional clear water jet is discharging over a movable bed with constant slope *S*. The model considers a two-phase flow: the fluid phase and the sediment phase. As a first approximation the sediment is treated as non-cohesive sediment with settling velocity v_s and submerged specific gravity *R*.
The mathematical model of the flow is based in the four-equation, depth-averaged model presented by Parker *et al.* [3] with the closure relations proposed by García and Parker [4]. In this model the flow is taken to be steady and fully turbulent, and the sediment concentration is assumed to be small in order for the Boussinesq approximation to be valid.

The important layer-averaged quantities are flow velocity *U*, volumetric concentration of suspended sediment *C*, layer thickness *h*, and level of turbulence *K* (layer-averaged value of turbulent kinetic energy). The equations governing the flow read as follows:

$$\frac{dUh}{dx} = w_e \tag{1}$$

$$\frac{dU^2h}{dx} = -\frac{1}{2}Rg\frac{dCh^2}{dx} + RgChS - u_*^2 \tag{2}$$

$$\frac{dUCh}{dx} = v_s(E_s - c_b) \tag{3}$$

$$\frac{dUKh}{dx} = u_*^2U + \frac{1}{2}U^2w_e - \varepsilon_0 h - Rgv_sCh - \frac{1}{2}Rgw_eCh - \frac{1}{2}Rgv_sh(E_s - c_b) \tag{4}$$

where u_*, E_s, w_e, c_b, and ε_0 are the bed shear velocity, the sediment entrainment coefficient, the water entrainment velocity, the near-bed sediment concentration, and the layer-averaged viscous dissipation, respectively.

The closure relations are taken as follows:

Bed shear stress:

$u_*^2 = C_D U^2$ for momentum-driven flow, $u_*^2 = \alpha K$ for buoyant-driven flow (5a, b)

where

$$C_D = 0.1\left(\frac{x}{2h_0}\right)^{-1}\left(\frac{U_0 2h_0}{\nu}\right)^{0.5} \text{ and } \alpha = 0.1$$

Here U_0 and h_0 are the initial conditions for the far field model (U_{2D} and h_{2D}), and ν is the kinematic viscosity of water. This relation has been taken from the work by Myers [6]. A new relation will be determined from measurement using the real sediment.

Sediment entrainment:

$$E_s = \frac{A z_u^{\,5}}{1+\frac{A}{0.3} z_u^{\,5}},\ A=1.3\ 10^{-7},\ z_u = \frac{u_*}{v_s} f(R_p),\ f(R_p) = \begin{cases} R_p^{\,0.6} & 3.5 \le R_p \\ 0.586 R_p^{\,1.23} & R_p \le 3.5 \end{cases} \quad (6)$$

Here $R_p = \frac{\sqrt{RgD_s}D_s}{\nu}$ is a Reynolds number defined using the characteristic sediment size D_s, the acceleration of gravity g and the submerged specific gravity of the sediment R.

Water entrainment:

$$w_e = e_w U, \quad e_w = \frac{0.075}{\left(1+718\,Ri^{2.4}\right)^{1/2}} \quad (7a, b)$$

where $Ri = \frac{RgCh}{U^2}$ is a bulk Richardson number.

Near bed suspended sediment concentration:

$$c_b = r_0 C, \quad r_0 = 1+31.5\left(\frac{v_s}{u_*}\right)^{1.46} \quad (8a, b)$$

TKE dissipation (should we solve an equation for epsilon?):

$$\varepsilon_0 = \beta\frac{K^{3/2}}{h}, \quad \beta = \frac{\frac{1}{2}e_w\left(1-Ri-2\frac{C_{D^*}}{\alpha}\right)+C_{D^*}}{\left(\frac{C_{D^*}}{\alpha}\right)^{3/2}} \quad (9a, b)$$

where C_{D^*} is a bed friction coefficient.

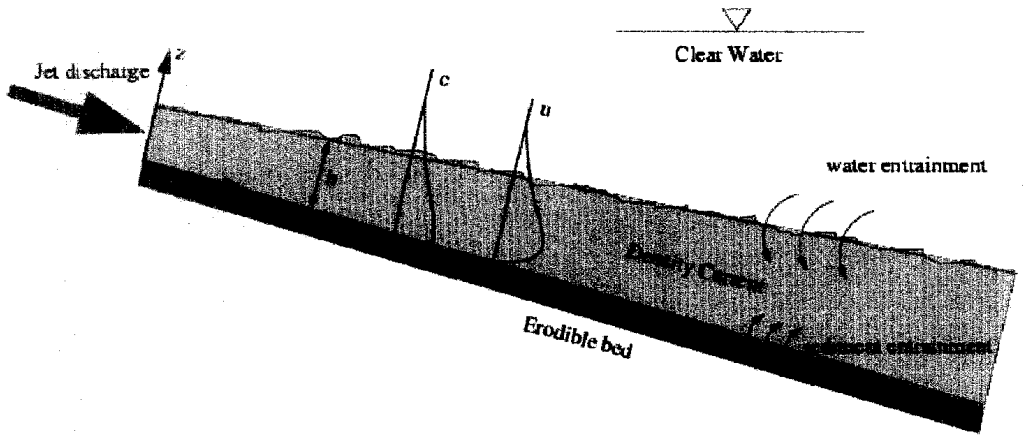

Figure 2. Schematic of a jet-induced density current over an erodible bed. The jet discharge induces an initial sediment resuspension that may lead to the development of a self-sustaining density current.

The coupling between phases is very important in the buoyant-driven flow region, and it is a key feature that dictates whether or not a self-sustained flow develops. This coupling occurs at different levels and scales. They are taken into account in the model in the buoyant term in the conservation of momentum (second term of the r.h.s. of equation 2), and in the closure for bottom shear stress by setting it proportional to the layer-averaged turbulent kinetic energy (equation 5).

Preliminary studies on the characterization of the sediment (see Appendix C) suggest that the sediment may behave as cohesive. In turn, it presents two different phases, one composed primarily by fine sediments, and the other composed by aggregated sediment. This also suggests that some characteristics of the sediment, such as density and settling velocity, may differ from one sediment phase to the other. More work is still needed in order to determine the shear and time scales for aggregate breakup and formation. Future work will consider a three-phase flow, a fluid phase and two sediment phases, in order to capture the cohesive behavior of sediment if needed.

References

[1] Knystautas, R., "The turbulent jet from a serie of holes in line". *The Aeronautical Quarterly*, vol. XV, 1964.

[2] Wang, J., Priestman, G., Wu, D., "An analytical solution for incompressible flow through parallel multiple jets". *Journal of Fluids Engineering*, vol. 123, 2001, 407-410.

[3] Parker, G., Fukushima, Y. and Pantin, H., "Self-accelerating turbidity currents". *JFM*, vol. 171, 1986, 145-181.
[4] García, M. H. and Parker G., "Experiments on the Entrainment of Sediment into Suspension by a Dense Bottom Current". *J Geoph. R*, vol. 98 (C3), 1993, 4793-4807.
[6] Myers 1961

APPENDIX C
Preliminary Report:
Characterization of solids from O'Hare reservoir

Abstract

Results of a series of experiments conducted to characterize sediment properties of solids from O'Hare reservoir are presented. The LISST-ST laser-diffraction instrument was used for the analyses. Different test samples were prepared from the solids provided by MWRD. Solid concentrations used in those samples varied between 2 and 20 ml/l. Tests with and without disaggregated samples were made in order to estimate the size of aggregate formation. The mean size of particles belonging to the original samples (not disaggregated) is about 24.5 μm, and the typical settling velocity is 0.05 cm/s, while corresponding values for disaggregated samples were 10.8 μm and 0.008 cm/s, respectively. Although more tests are needed, the results obtained so far indicate a negligible dependence of the settling velocity on sediment concentration and this applies to both the original and disaggregated samples. The mean size of the aggregates found in the original sediment samples (not disaggregated) was estimated indirectly, from particle size and concentration distributions measurements. The results indicate that the mean diameter of the aggregates is about 84 μm with a mean settling velocity of 0.5 cm/s. Given the range of particles sizes found in this preliminary study, it is concluded that this sediment can be considered as cohesive.

Theoretical aspects of cohesive sediment

Cohesive sediment is composed predominantly by silt and clay, with particle sizes less than 62 μm. In this size range inter-particle physico-chemical forces exist, which may exceed the effect of gravitational forces. Because of this, cohesive particles tend to attach to each other, forming aggregates or flocs as a result of particle-particle interactions.

Flocculation is a phenomenon involving the formation of flocs and their subsequent settling. Through flocculation, even the finest material transported in suspension in a water flow (silts and clays) can eventually get deposited on the bottom, in cases for which those fine particles would never reach the bed through sedimentation as individual particles.

The process of aggregation is defined as a set of mechanisms by which floc size, density and strength (resistance to breakup or disaggregation) are established, as functions of cohesion, size and organic content. Such process depends also on flow-particle and particle-particle (or floc-floc) interactions. A floc may originate in the water column or just above the bed. There it may deposit to the soft mud layer and become part of bed, or

it may be broken into smaller particles which are picked up by the flow to begin a new flocculation process.

Flocs or aggregates are formed by the attachment of a number of sediment particles that get together due to collisions. This flocculation process is governed mainly by three processes:

1. Brownian motion of fluid molecules, which causes collisions between them and individual solid particles, exerting forces that move the particles in random directions increasing the chances for particle-particle collisions.
2. Small-scale turbulent eddies exert drag forces that, like Brownian motion, impart random motion to particles of sizes similar to those eddies.
3. Differential settling, associated to different particles sizes having different settling velocities. This effect may increase or decrease flocculation, depending on how high the concentration of sediment is. Particles with large settling velocities tend to overtake particles with smaller settling velocities, such that collisions between these particles may result in flocculation.

Factors that enhance the flocculation and the floc sizes are, for instance, increasing concentrations of sediment and organic content, which makes the binding forces between particles large. With increasing organic content flocs become larger, but their density decreases. In still water, due to differential settling, the flocs may grow to larger sizes compared with those in a turbulent flow situation. Other factors that affect the flocculation are salinity and temperature of water.

Flocculation occurs for particle sizes smaller than about 10-15 microns, in combination with large concentrations. Flocculation is dominant for concentrations between 300 mg/l and 1000 mg/l. For smaller concentrations flocculation processes still exist although they are of smaller importance (Krone, 1962).

Shearing forces larger than the strength of flocs can break them up. Large shearing forces usually exist near the bottom of water currents where the velocity gradients are larger than in the rest of the water column. Also large shearing forces exist within small eddies distributed everywhere in the fluid. Indeed, in turbulent flows, fluctuating forces may produce a continuous process of flocculation and break-up resulting in a dynamic equilibrium of the flocs size and concentration.

Experimental research regarding cohesive sediment suspensions in annular flumes has produced the following main conclusions:

-The lower the particle concentration, the lower the flocculation.
-Shear velocities near the bottom control flocs deposition and erosion.
-τ_{bc}: critical bottom shear stress (τ_b) below which the flocculation process begins. Lower values of the bed shear stresses ($\tau_b < \tau_{bc}$) imply flocculation.
-τ_{bfull} : bottom shear stress below which all sediment is deposited by flocculation.
-τ_{bc} and τ_{bfull} depend on the type of sediment.

Different researchers have found different values of the threshold shear stresses τ_{bc} and τ_{bfull}, depending on type of sediment and water salinity. A summary of these results is presented in Table 1.

Table 1 Summary of limit shear stresses for deposition by flocculation according to different studies

Researchers	Concentration (mg/l)	Facility	Sediment	Type of water	τ_{bfull} (N/m^2)	τ_{bc} (N /m^2)
Mehta y Partheniades (1975)	300 a 10000	Annular flume (laboratory)	Kaolin	Distilled	0.15	-
Krone 1962)	< 300	Annular flume (laboratory)	-	-	-	0.06
Mehta (1984) & Winterwerp (1991)	100 a 1000	Anular flume (laboratory)	Kaolin	Distilled	0.15	1 4
Mehta (1984) & Winterwerp (1991)	100 a 1000	Anular flume (laboratory)	Lakes and rivers of Holland	-	0.06 to 0.1	-
Partheniades (1986)	100 a 300	Anular flume (laboratory)	San Fransisco Bay	Ocean	-	0.065 to 0.07

Methodology and Instrumentation

Different techniques exist for measuring particle size distribution and settling velocity. In this study a laser-diffraction instrument, LISST-ST was used. This instrument measures size distribution, concentration, and settling velocity distribution of suspended particles. The main advantage of using the LISST-ST is that no assumption of particle density is necessary for determining the aforementioned variables. The range of particle sizes measured by LISST-ST (Type B) is 1.25 to 250 μm. A multi-angle technique is used by LISST-ST, relating scattering angle to particle size. Diffracted laser light is collected in several rings and the diameters of these rings vary logarithmically as presented in Fig. 1. Large particles are described by small angles and consequently belong to inner rings. Since the diameter of these rings varies logarithmically, the size classes are also ordered logarithmically. These size classes are shown in Fig. 2.

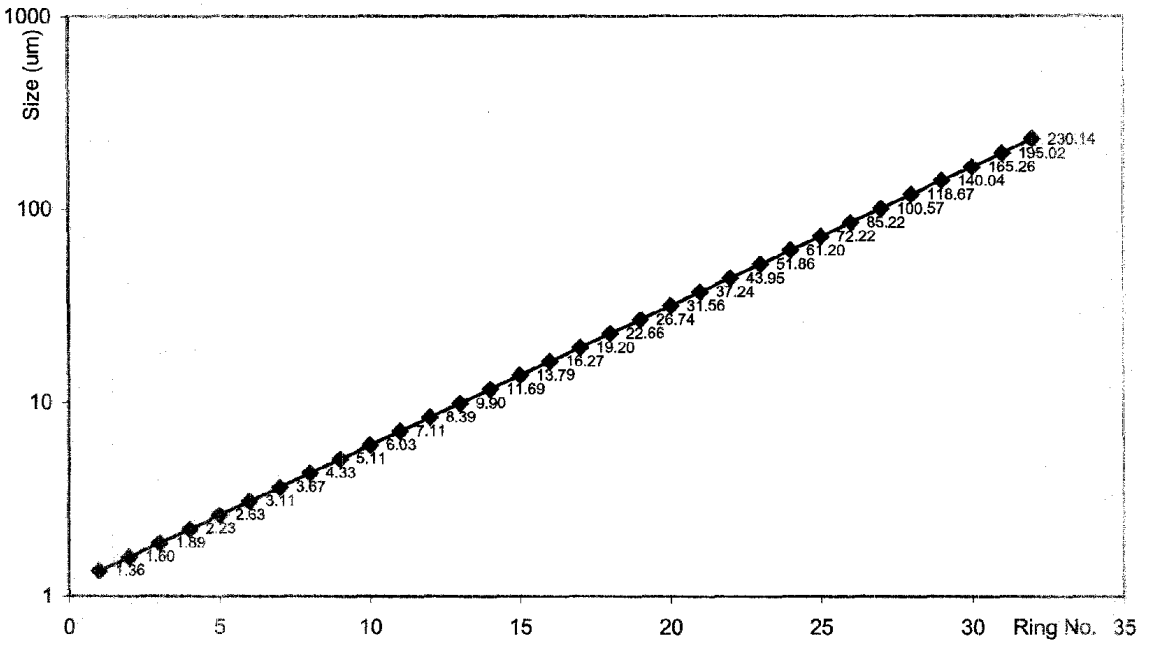

Fig. 1: Mean size of the Ring

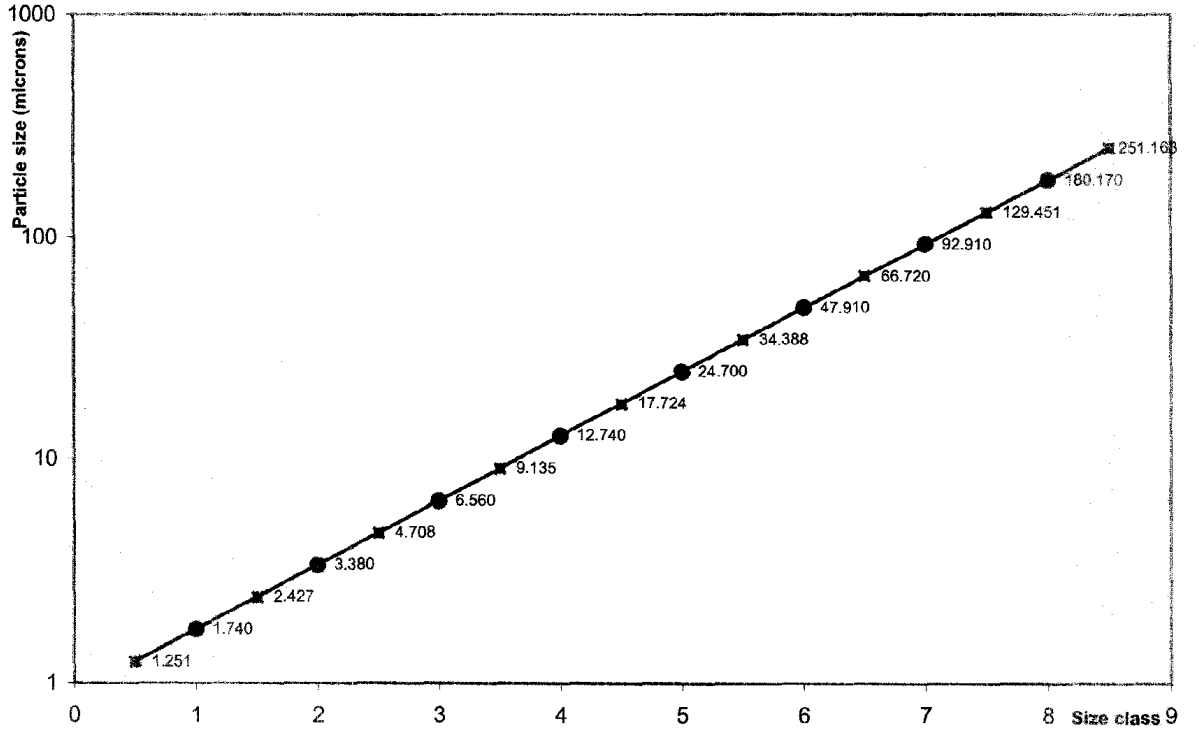

Fig. 2: Size class vs. Particle sizes

Samples of water-solid mixtures with different concentrations were prepared using solids from O'Hare reservoir provided by MWRD. Two different types of samples were prepared: disaggregated and non-disaggregated, denoted McD and Mc, respectively. The disaggregated samples were created by means of mechanical mixing and blending of water-solid mixtures using the solids provided by MWRD, in order to break down and eliminate aggregates and flocs that are originally present in those solids. Using the LISST instrument, the samples were analyzed to obtain particle size distributions and corresponding particle settling velocities.

Data analysis

Particle size distribution

The particle size distribution associated with each sample of both series Mc and McD, and their corresponding concentration, is shown in Table 2 and Fig. 3.

Table 2. Particle-Size Distribution

Particle Diameter (μm)	1.74	3.38	6.56	12.74	24.7	47.91	92.91	180.17	Total Conentration (μl/l)
Sample	% Finer								
Mc1	8.26	27.76	44.66	60.63	76.60	90.53	95.26	100.00	5385
Mc2	12.12	33.12	51.21	66.56	80.37	92.49	96.45	100.00	6190
Mc3	14.30	35.49	53.36	67.91	81.44	91.80	96.09	100.00	19585
Mc4	17.99	37.46	53.82	67.83	80.53	89.10	93.38	100.00	12840
Mc5	27.65	41.47	57.09	71.68	83.21	91.40	96.16	100.00	1953
Mc6	25.66	42.36	56.09	69.45	81.74	90.69	94.93	100.00	8380
McD1	27.20	49.07	69.33	81.87	90.93	96.27	98.35	100.00	18750
McD2	26.00	52.35	73.15	86.32	95.82	99.15	99.69	100.00	14423
McD3	23.91	49.11	70.44	84.65	94.73	98.80	99.52	100.00	15475
McD4	23.60	48.89	69.80	83.96	94.08	98.13	99.02	100.00	14828
McD5	24.95	50.19	71.87	85.95	95.57	98.87	99.47	100.00	16830
McD6	19.91	46.46	69.03	83.63	94.25	98.36	99.20	100.00	11300
McD7	18.85	46.45	66.96	82.49	94.71	98.63	99.20	100.00	6631
McD8	18.18	45.90	67.54	82.61	93.96	98.37	99.20	100.00	5774
McD9	18.38	44.07	65.15	80.29	93.81	99.08	99.54	100.00	3669

Fig. 3 reveals that the particle size distribution of the McD samples is finer than that of the Mc samples. The McD samples show an amount of clay-size material between 22% and 32% in weight while those values decrease to between 10% and 29 % for the Mc samples.

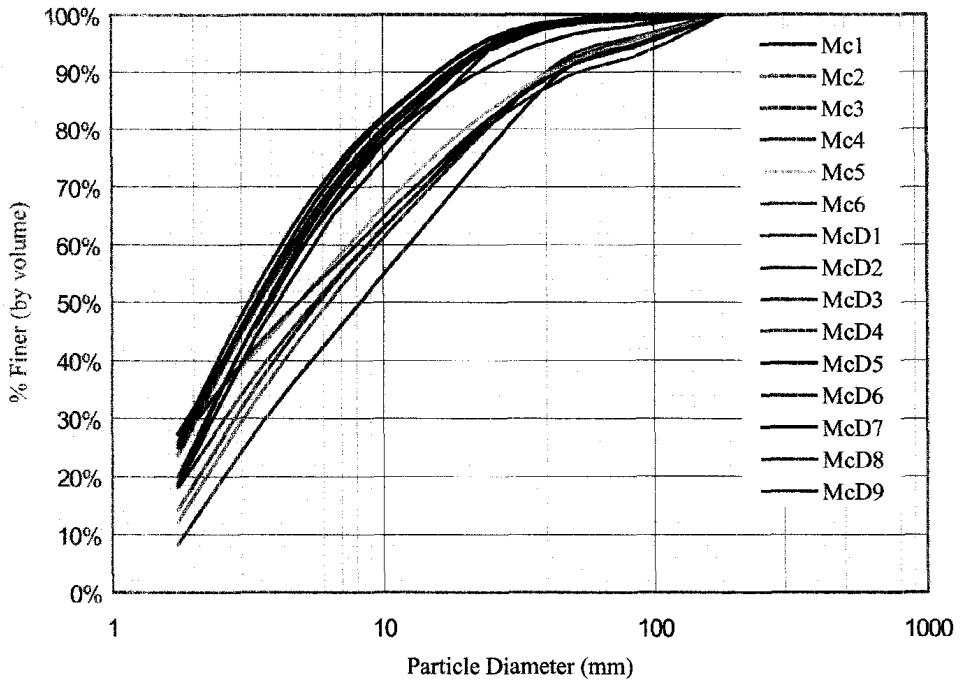

Fig. 3. Particle-Size Distribution

Settling velocity

A summary of the settling velocity of each particle size fraction for each of the samples tested, obtained using the LISST instrument is shown in Tables 3 and 4.

Table 3. Settling velocity of Mc samples (cm/s)

Particle Diameter (μm)	1.74	3.38	6.56	12.74	24.7	47.91	92.91	180.17
Mc1	5.46E-04	2.44E-03	4.32E-03	1.69E-02	5.44E-02	2.59E-01	6.85E-01	8.33E-01
Mc2	4.78E-04	1.65E-03	3.56E-03	9.42E-03	3.03E-02	1.44E-01	3.82E-01	8.33E-01
Mc3	6.92E-04	1.25E-03	2.11E-03	1.14E-02	4.48E-02	2.13E-01	6.85E-01	8.33E-01
Mc4	3.18E-04	3.56E-03	4.32E-03	1.39E-02	4.48E-02	1.19E-01	3.14E-01	6.85E-01
Mc5	1.95E-04	2.53E-04	7.60E-04	7.75E-03	4.48E-02	3.14E-01	8.33E-01	2.59E-01
Mc6	1.95E-04	8.43E-04	9.46E-04	7.75E-03	3.03E-02	1.44E-01	5.64E-01	1.01E+00
Mean Value	4.04E-04	1.67E-03	2.67E-03	1.12E-02	4.16E-02	1.99E-01	5.77E-01	7.42E-01

Table 4. Settling velocity of McD samples (cm/s)

Particle Diameter (μm)	1.74	3.38	6.56	12.74	24.7	47.91	92.91	180.17
McD1	8.92E-04	1.65E-03	2.89E-03	7.75E-03	2.50E-02	2.13E-01	2.21E+00	
McD2	6.35E-04	1.49E-03	2.11E-03	6.38E-03	1.69E-02	4.48E-02	2.13E-01	
McD3	6.92E-04	1.65E-03	2.11E-03	6.38E-03	2.05E-02	8.03E-02	3.82E-01	
McD4	7.60E-04	1.49E-03	2.11E-03	1.14E-02	3.69E-02	1.75E-01	8.33E-01	
McD5	1.36E-03	1.85E-03	2.89E-03	1.14E-02	3.03E-02	8.03E-02	2.59E-01	3.14E-01
McD6	7.60E-04	1.49E-03	2.44E-03	7.75E-03	2.05E-02	6.61E-02	2.59E-01	3.14E-01
McD7	5.10E-04	1.65E-03	1.65E-03	1.14E-02	3.69E-02	9.76E-02	1.44E-01	1.75E-01
McD8	5.10E-04	1.36E-03	1.85E-03	1.14E-02	3.03E-02	9.76E-02	4.64E-01	
McD9	1.95E-04	1.25E-03	2.11E-03	1.39E-02	3.69E-02	2.59E-01	2.59E-01	1.44E-01
Mean Value	7.02E-04	1.54E-03	2.24E-03	9.76E-03	2.82E-02	1.24E-01	5.58E-01	2.37E-01

Mean diameter and mean settling velocity

The computed d_{50}, mean diameter, dm, and settling velocity associated with dm, ws, of each of the samples of series Mc and McD are shown in Tables 5 and 6, respectively. For the Mc samples, these results show a variation of d_{50} in the range 5.2 to 8.1 μm, with a mean value of about 6.0 μm, and a variation of dm in the range 23.3 to 27.5 μm, with a mean value of about 24.5 μm. The corresponding settling velocity is in the range 0.03 to 0.07 cm/s with a mean value of about 0.05 cm/s. For the disaggregated samples (series McD) the d_{50} values show a slight variation in the range 3.2 to 4.0 μm, with a mean value of about 3.3 μm, while the dm values are in the range 8.8 to 12.2 μm, with a mean value of about 10.8 μm. The corresponding settling velocity is in the range 0.004 to 0.012 cm/s with a mean value of about 0.008 cm/s.

Table 5 Mean Diameter, weighted mean diameter and weighed mean settling velocity of Mc samples

Sample	d_{50} (μm) (1)	dm (μm) (2)	Ws (cm/s) (3)
Mc1	8.1	23.32	0.050
Mc2	6.2	23.36	0.028
Mc3	5.8	27.49	0.070
Mc4	5.5	26.98	0.070
Mc5	5.2	21.95	0.035
Mc6	5.15	24.01	0.029
Mean	6.00	24.52	0.047

Table 6 Mean Diameter, weighted mean diameter and weighed mean settling velocity of Mc samples

Sample	d_{50} (μm) (1)	dm (μm) (2)	Ws (cm/s) (3)
McD1	3.4	10.9	0.007
McD2	3.3	8.8	0.004
McD3	3.2	9.6	0.004
McD4	3.2	11.5	0.009
McD5	3.2	9.7	0.008
McD6	3.3	11.5	0.007
McD7	3.7	11.4	0.009
McD8	3.7	11.62	0.010
McD9	4	12.18	0.012
Mean	3.3	10.8	0.008

In general, this sediment can be characterized as silty clay, with a mean content of clay-size material of about 27 % and with about 50% in weight of particles smaller than 10 μm, for both Mc and McD samples. This value, 10 μm, corresponds to the particle size below which it is considered that the sediment has cohesive properties and is affected by flocculation-driven settling.

Figure 4 shows a plot of the mean settling velocity, ws, as a function of the mean diameter, dm, of each of the samples tested in the Mc and McD series (values from columns (2) and (3) in Tables 5 and 6).

As it is apparent from Fig.4, the settling velocity obtained for both the Mc and McD samples does not show a strong tendency to change with concentration, although in the former case ws tends to slightly increase as the concentration increases. What is clear is that the Mc samples exhibit a larger settling velocity (about 0.05 cm/s) than the McD ones (about 0.008 cm/s). This simply responds to the larger values of dm observed in those samples with respect to the disaggregated ones. These results indicate that aggregates are present in the solids obtained from O'Hare reservoir. Those aggregates increase the mean diameter of the sediment samples and also increase the mean settling velocity of the solids.

Mean-Size of Aggregates in McCook samples

In order to estimate the mean size of flocs or aggregates in the solids samples from O'Hare reservoir, an indirect analysis was done. Tables 7 and 8 show the concentration corresponding to each particle size fraction in the Mc and McD samples.

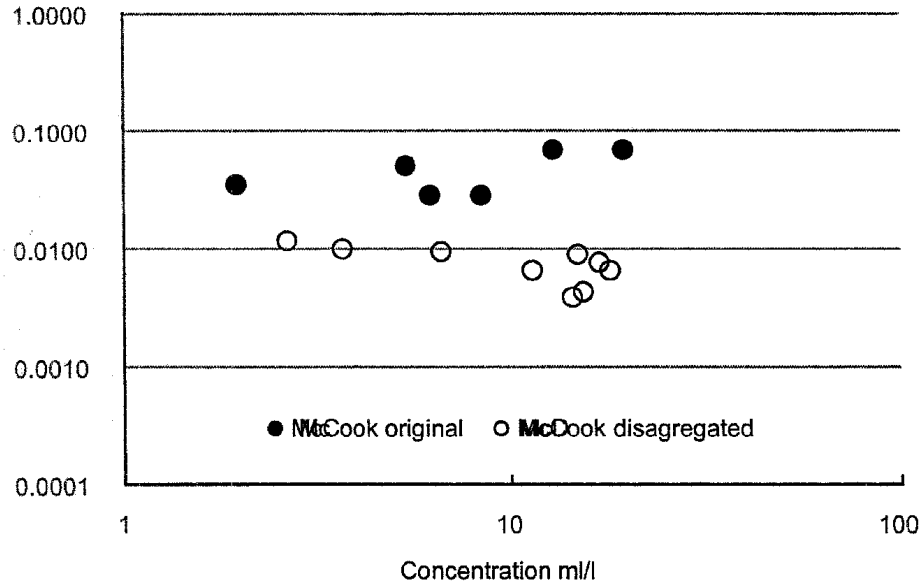

Fig.4 Mean settling velocity versus concentration

Table 7 Concentrations for Mc Samples

	Total concentrations								Total Conc. ul/l
	1.74	**3.38**	**6.56**	**12.74**	**24.7**	**47.91**	**92.91**	**180.17**	
Mc1	8.26%	19.50%	16.90%	15.97%	15.97%	13.93%	4.74%	4.74%	5385
Mc2	12.12%	21.00%	18.09%	15.35%	13.81%	12.12%	3.96%	3.55%	6190
Mc3	14.30%	21.19%	17.87%	14.55%	13.53%	10.37%	4.29%	3.91%	19585
Mc4	17.99%	19.47%	16.36%	14.02%	12.69%	8.57%	4.28%	6.62%	12840
Mc5	27.65%	13.82%	15.62%	14.59%	11.52%	8.19%	4.76%	3.84%	1953
Mc6	25.66%	16.71%	13.72%	13.37%	12.29%	8.95%	4.24%	5.07%	8.38
Mean Mc	17.66%	18.62%	16.43%	14.64%	13.30%	10.35%	4.38%	4.62%	9055

Table 8 Concentrations for McD Samples

	Total concentrations								Total Conc. ul/l
	1.74	3.38	6.56	12.74	24.7	47.91	92.91	180.17	
McD1	27.20%	21.87%	20.27%	12.53%	9.07%	5.33%	2.08%	1.65%	18750
McD2	26.00%	26.35%	20.80%	13.17%	9.50%	3.33%	0.54%	0.31%	14423
McD3	23.91%	25.20%	21.32%	14.22%	10.08%	4.07%	0.71%	0.48%	15475
McD4	23.60%	25.29%	20.91%	14.16%	10.12%	4.05%	0.89%	0.98%	14828
McD5	24.95%	25.25%	21.68%	14.08%	9.62%	3.30%	0.59%	0.53%	16830
McD6	19.91%	26.55%	22.57%	14.60%	10.62%	4.12%	0.84%	0.80%	11300
McD7	18.85%	27.60%	20.51%	15.53%	12.22%	3.92%	0.57%	0.80%	6631
McD8	18.18%	27.71%	21.65%	15.07%	11.34%	4.42%	0.83%	0.80%	5774
McD9	18.38%	25.68%	21.09%	15.14%	13.52%	5.27%	0.46%	0.46%	3660
Mean McD	22.33%	25.72%	21.20%	14.28%	10.68%	4.20%	0.84%	0.76%	11963

The difference between mean concentrations in McD and Mc samples corresponding to the same particle size fraction is shown in Table 9.

Table 9 Difference between concentrations in Mc and McD samples

Particle Diameter (um)	1.74	3.38	6.56	12.74	24.7	47.91	92.91	180.17
Mean McD – Mean Mc	4.67%	7.11%	4.77%	-0.36%	-2.63%	-6.15%	-3.54%	-3.86%

The mean concentration difference, in percentage, between McD and Mc samples shown in Table 9 is positive for particle size fractions smaller than 12.74 μm and negative otherwise. This result indicates that there is a larger amount of particles with a size smaller than 9.135 μm (which is the upper limit of the size fraction that has 6.56 μm as mean diameter) in the McD samples than in the Mc samples. The smaller particles present in the disaggregated samples, apparently, take part in the aggregate formation in the Mc samples.

A graphic version of this analysis is shown in Fig 5.

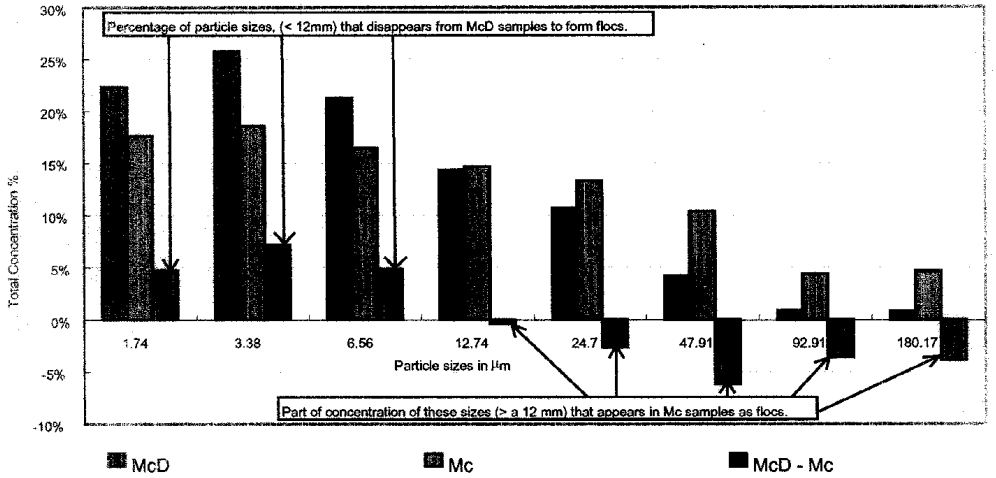

Figure 5: summary of aggregate analysis

As shown in Table 10, the accumulated concentration difference between samples McD and Mc in the range of sizes 1.74 to 6.56 µm is 16.55%.

Defining I as:

Where Mean Mc denotes the mean concentration of a particular size fraction in the Mc samples and Mean McD denotes the mean concentration of the same size fraction in the McD samples. The values of I obtained from the present analysis in the range of sizes 12.74 to 180.17 µm are shown in Table 11. The accumulated value of 16.55% represents an estimation of the amount of floc concentration in Mc samples.

Table 10 Increment of particle concentration in the range of sizes between 1.74 to 6.56 µm in series McD with respect to Mc

Particle Diameter µm	1.74	3.38	6.56	
Mean McD – Mean Mc	4.67%	7.11%	4.77%	16.55%

Table 11 Increment of particle concentration in the range of sizes between 12.74 to 180.17 µm in series Mc with respect to McD

Particle Diameter µm	12.74	24.7	47.91	92.91	180.17	
Mean Mc – Mean McD	0.36%	2.63%	6.15%	3.54%	3.86%	16.55 %
(Mean Mc – Mean McD) / Mean Mc	2.48%	19.75%	59.43%	80.91%	83.60%	

Mean Diameter of Flocs

Using Table 11, the mean floc diameter in the samples from O'Hare reservoir was calculated from a weighed average considering the percentage (Mean Mc – Mean McD) in which the mean concentration in each size range increases due to the presence of flocs. The mean diameter of flocs present in the solids from O'Hare reservoir is 84 µm and its corresponding settling velocity is 0.5 cm/s.

APPENDIX D

Cohesive Sediment Experiments in Laboratory with Annular Flume

Introduction

The processes of deposition, consolidation, and erosion of cohesive sediment are controlled by a complex array of physical and chemical factors that are only partly understood. As yet it is not possible to predict the behavior of cohesive sediments from their physical and chemical properties alone, and some empirical relations must be develop for engineering computations. The annular flume has been recognized as the appropriate apparatus in the investigation of the properties of cohesive sediments.

Materials

Annular Flume

The annular flume consists of a ring-shaped flume in which the flow is driven by the differential motion of the ring in contact with the fluid and the channel (see figure 1). The use of annular flumes has several advantages in cohesive sediment research. The motion to the fluid is transmitted by mean of wall roughness, which prevents flocs to be broken up by pumps. In this way the aggregate structure of the suspended sediment is preserved during the experiment (Krishnappan 1993). In addition, since there is no inflow or outflow condition; once steady state is achieved; the flow is fully developed over the entire bed (Spork et al 1993).

The annular flume used in this study was constructed by Engineering Laboratory Design, Inc. of Lake City, Minnesota. The channel is made of laminated fiberglass and it has one Plexiglas window. It is supported by a five-leg frame of welded steel structural tubing. The flume rests on an aluminum board with a steel ring that runs on five rollers. The flume has an inner radius of 55 cm, an outer radius of 75 cm, and is 45 cm deep. Seven taps were installed at 5-cm intervals on the outer wall of the flume in order to take water samples at heights ranging from 5 to 35 cm. Another tap installed at a height of 18 cm was used to add clean water to the flume after samples were taken so that the volume of water inside the flume remained constant. Figure 2 is a photograph of the sampling taps.

The lid is made of Plexiglas bolted to a steel frame mounted on a threaded shaft. The lid can be moved up and down on this shaft to allow for flow depths between 20 and 40 cm, and a large nut holds it at the desired vertical position. Three holes were cut into the lid in order to insert various measuring devices into the flow. The holes were sealed with Plexiglas caps when not in use. A painted wooden shelf was put on the support arms of the lid to hold a laptop computer and the data logger for the ADV.

The lid and the channel are each equipped with a digital signal conditioner manufactured by Electro-Sensors. The convert shaft speed measured with magnetic sensors to analog

Methods

Description of experiments

Two types of experiments are going to be performed with the annular flume: deposition tests and erosion tests. In a deposition test, the flume is first set to a high speed to ensure complete mixing throughout the water column. Then the speed of the flume is quickly lowered to the desired setting. The evolution of the suspended sediment profile is usually measured periodically by taking samples from the flume, and then adding clean water so that the total volume remains constant. The results of deposition test indicate how much sediment stays in suspension for a given bed shear stress and bulk concentration of sediment.

While deposition tests begin with a water-sediment slurry, erosion tests start with a flat bed previously deposited by a water-sediment slurry. Suspended sediment concentration is monitored for a given bed shear stress. Once equilibrium has been reached, the shear stress is abruptly increased. Resuspension tests measure the critical shear stress for erosion, as well as the erosion rates for different bed shear stresses (Lau and Droppo 2000).

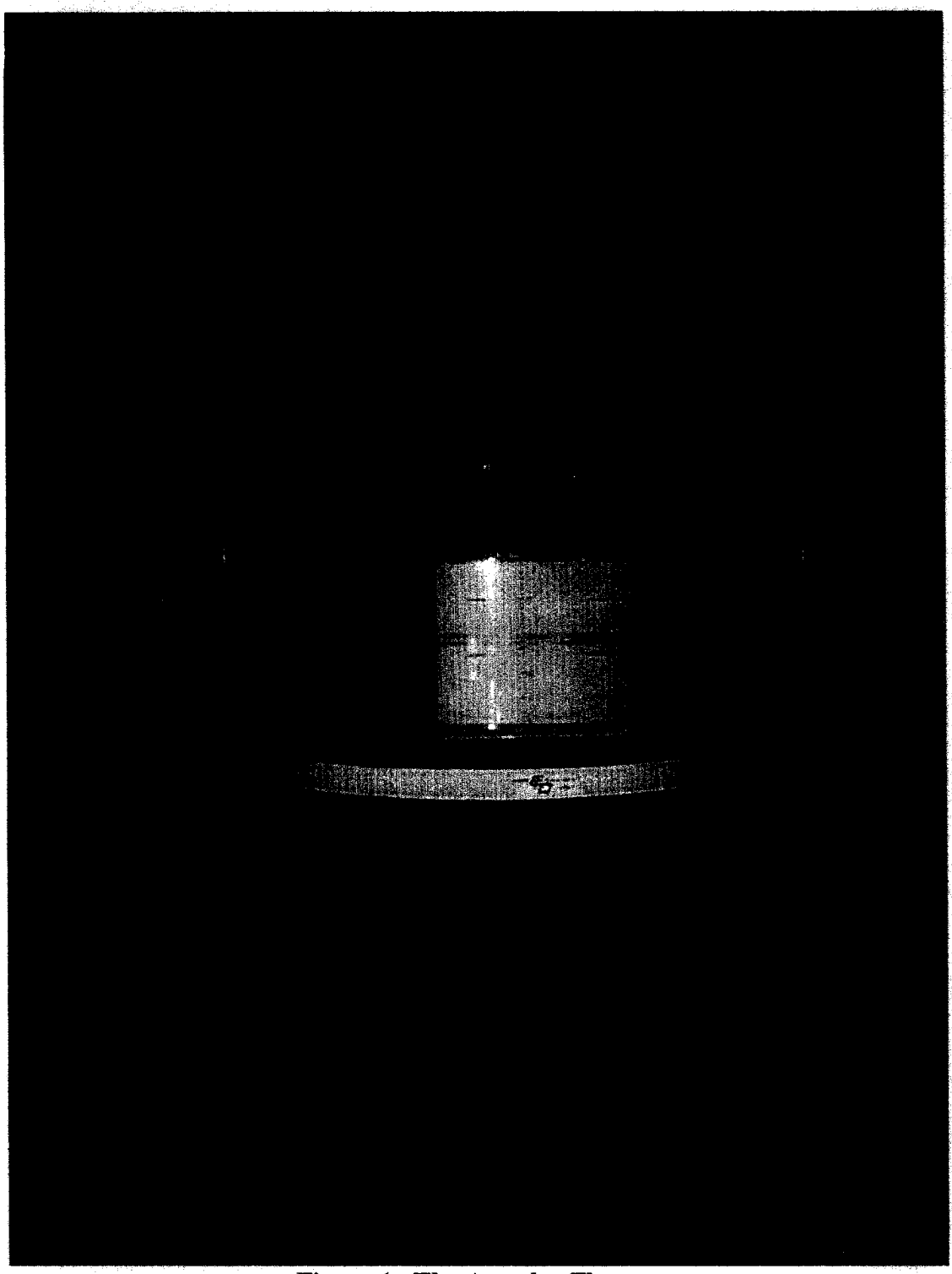

Figure 1. The Annular Flume.

Figure 2. Sampling Taps.

APPENDIX E

Flow structure in the near field of parallel wall jets in McCook reservoir. Numerical simulations using FLOW3D

Jets configuration:

Nozzle diameter: $d = 0.10$ m
Pitch: $s = 1.00$ m
Jet velocity: U_0: 1 m/s
X domain: 10 m (100 cells)
Y domain: 5.0 m (100 cells)
Z domain: 2.0 m (30 cells)

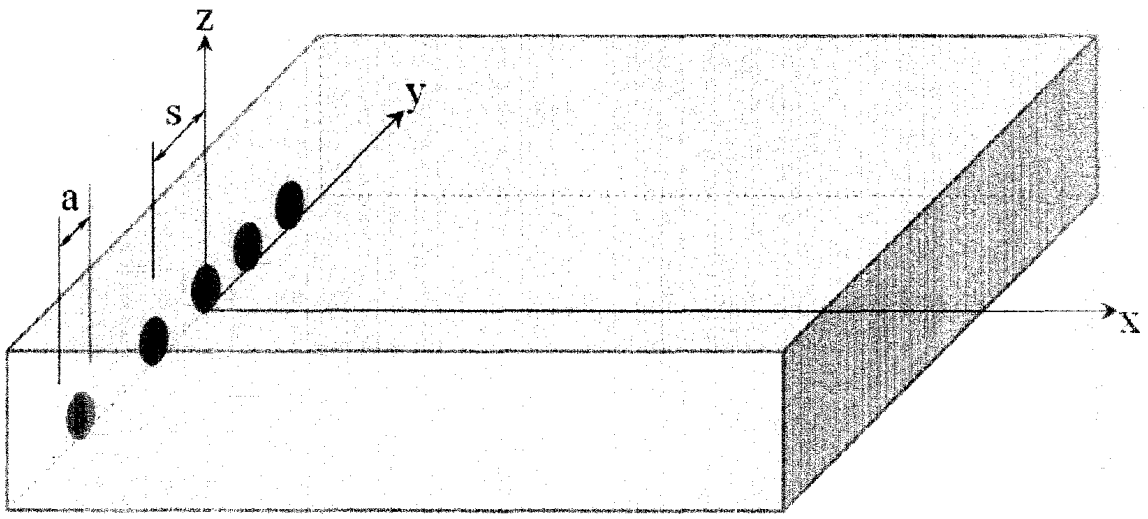

Fig. 1 Parallel wall jets configuration

Results:

The results obtained are plotted at 30 seconds, when the flow field generated by the jets is still developing.

Figs. 2 to 5 show a top view of the flow field (x - y plane) at different elevations in z (vertical).

Fig. 6 shows the flow field in the x - z plane for the three central jets (at y = -2.0 m, y = -1.0 m, and y =0.0 m) and cross sections ($y - z$ planes) at different x positions.

The color code for the plots of the velocity field is in Fig. 6.

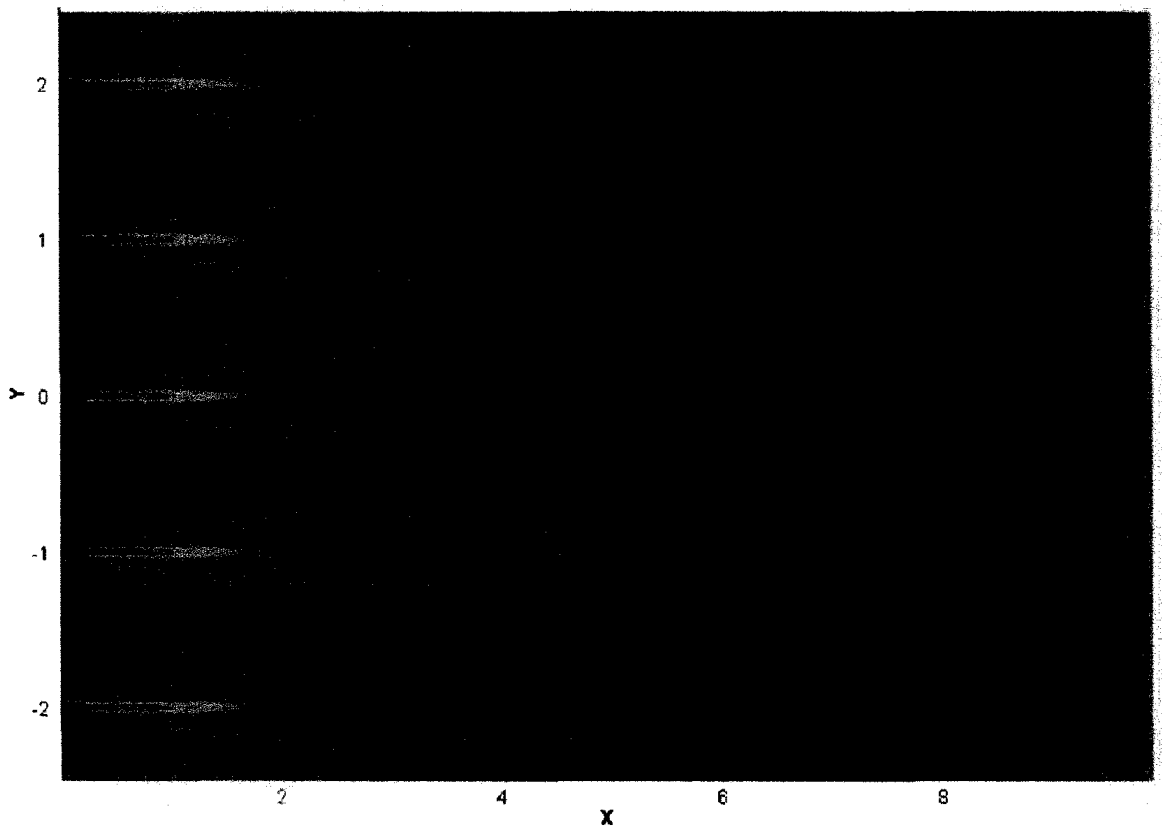

Fig. 2 Plan view of the flow velocity field at K = 1: z = 0.017 m from the bottom wall.

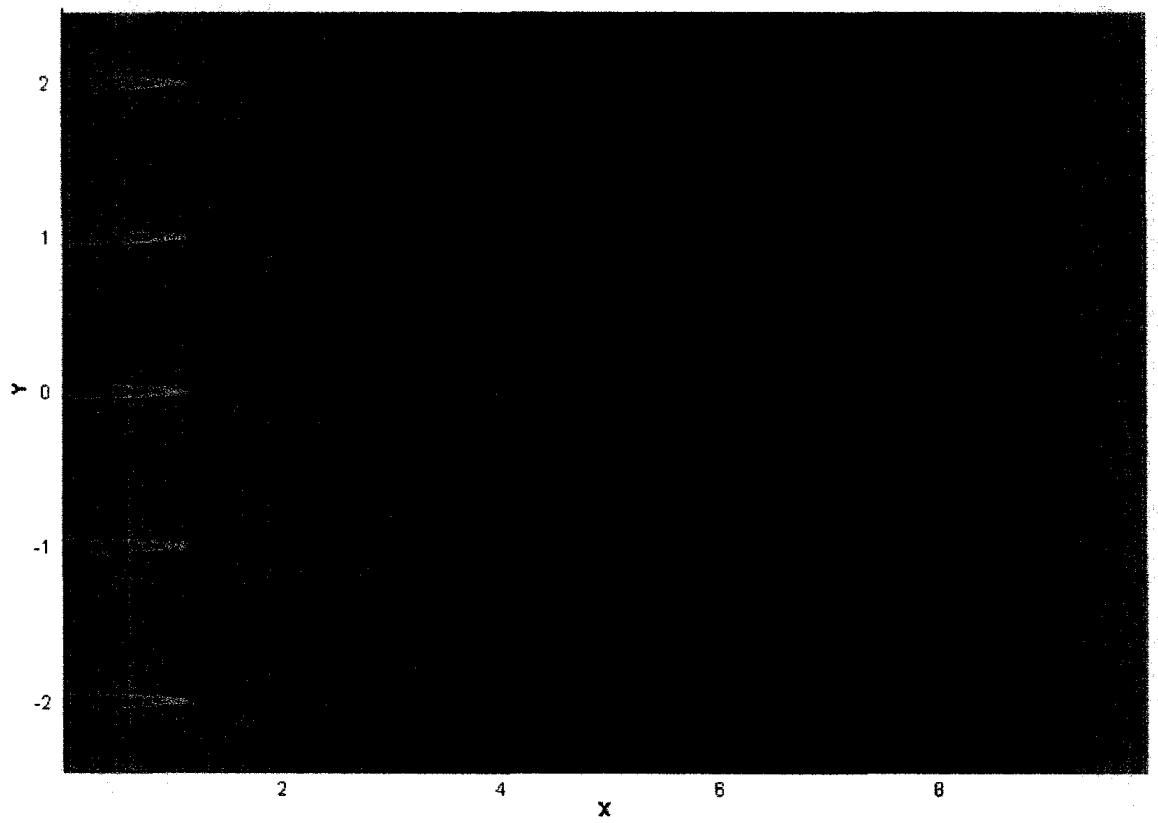

Fig. 3 Plan view of the flow velocity field at K = 2: $z = 0.05$ m from the bottom wall.

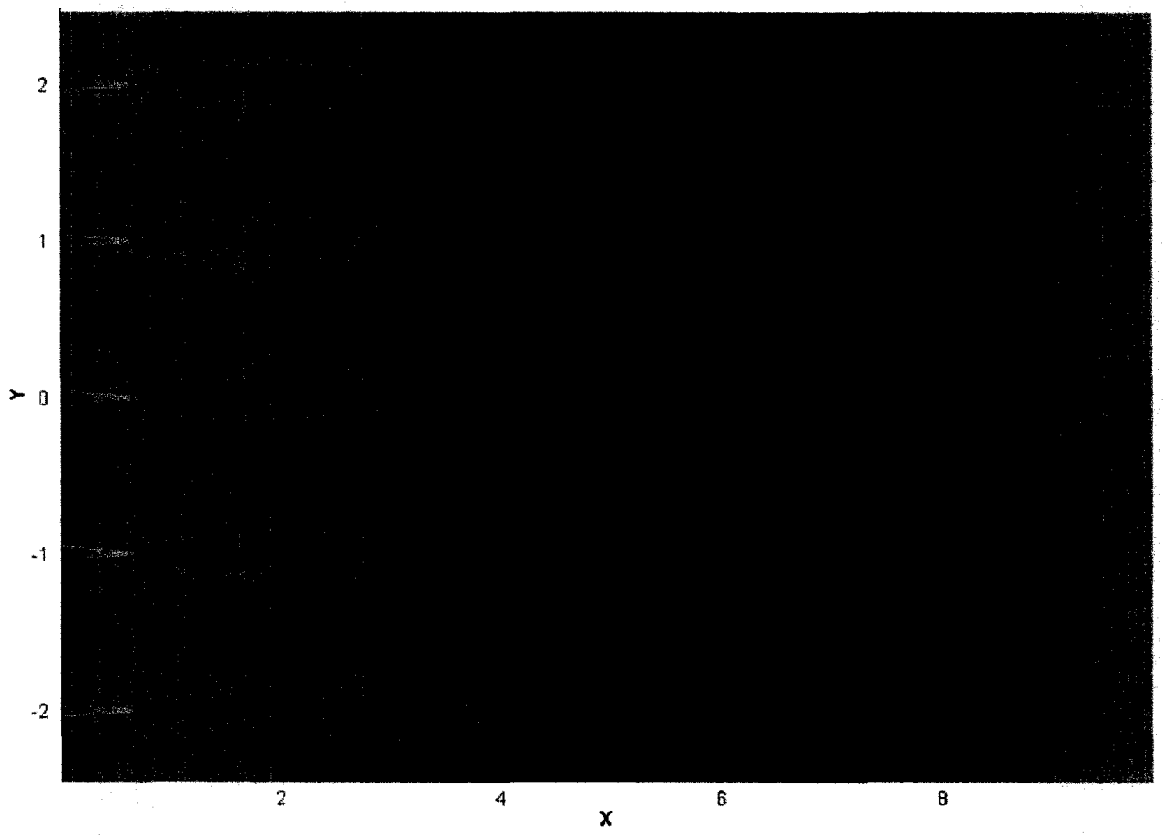

Fig. 4 Plan view of the flow velocity field at K = 3: $z = 0.083$ m from the bottom wall.

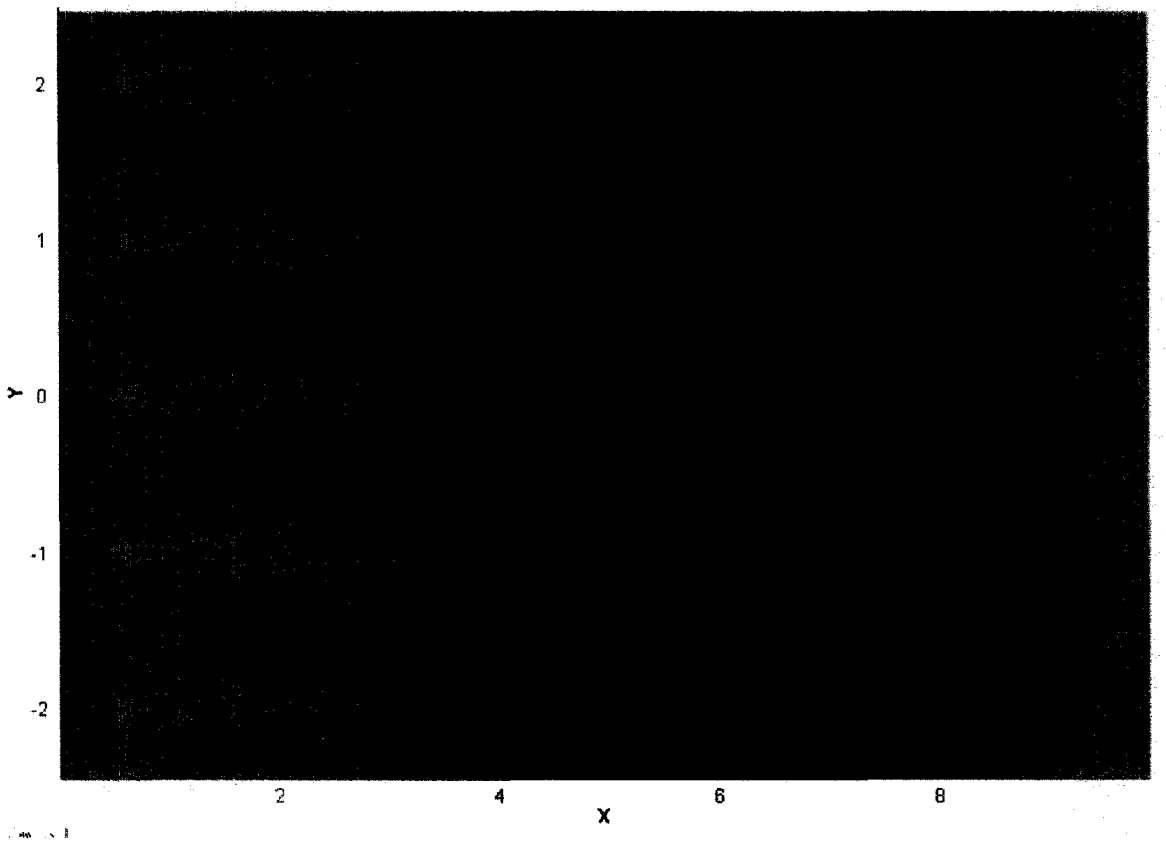

Fig. 5 Plan view of the flow velocity field at K = 4: $z = 0.117$ m from the bottom wall.

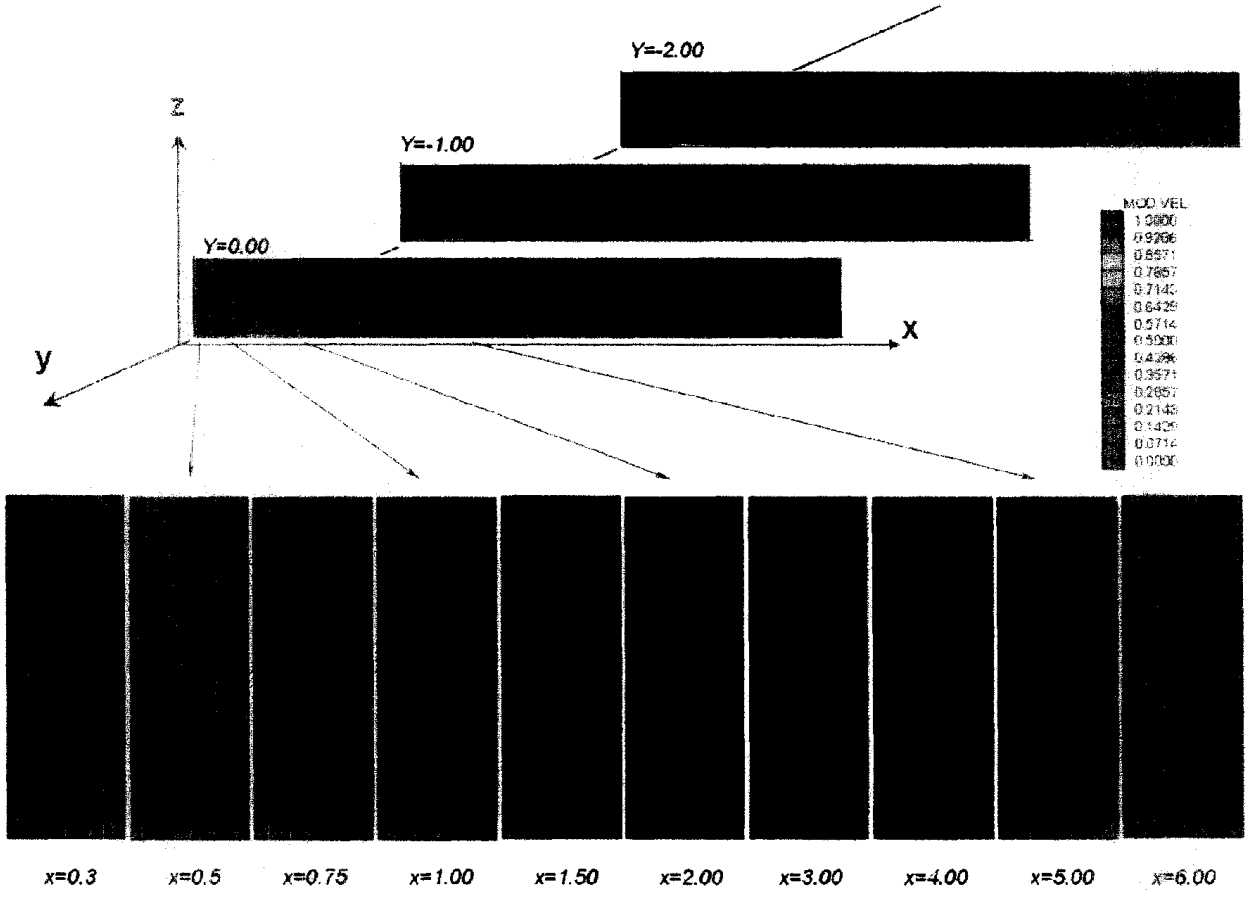

Fig.6 Flow field in the three central jets ($x - z$ planes) and cross sections (y - z planes) at different x positions.

APPENDIX F

Experimental study on flow structure and erosion in the near field of jets

Experiments

The experiments are being conducted in an existing water tank (7.3 m by 2.7 m horizontal area and 2.3 m height) having a plate 5.4 m long and 2.5 m wide, with adjustable slope, representing the bottom of McCook reservoir. A partition that generates a channel 0.3 m wide is being used with a bottom slope of about 1.5%. A plane wall jet is discharged into the channel, parallel to the bottom (Fig. 1). Two different situations are being analyzed using either a fixed bottom or a movable bed formed with a fine quartz material provided by U.S. Silica Company, having a mean size of about 19 to 45 μm. During the experiments the flow field generated by the jet discharge is monitored by means of an array of 4 synchronized ADVs (Acoustic Doppler Velocimeter). Erosion rates are registered by means of video recordings of the erosion process. Sediment concentrations generated by the entrainment process are measured through samples taken from the water column.

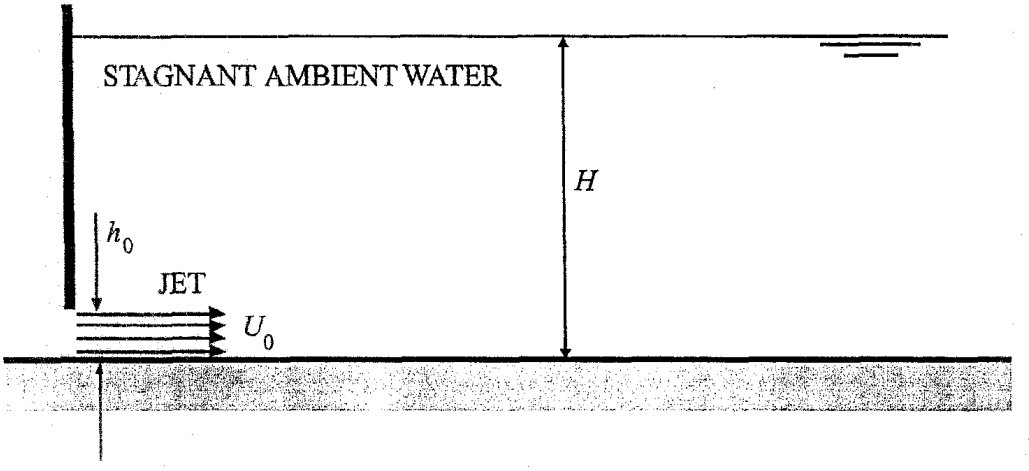

Fig. 1 Plane wall jet parallel to channel bottom.

Flow structure in the near field of plane wall jet

An example of the results obtained, corresponding to the flow velocity structure induced by a wall jet parallel to a fixed bottom, is shown in Fig. 2. The jet flow velocity was $U_0 = 0.73$ m/s and the jet height $h_0 = 0.0225$ m, which define a value of the jet Reynolds number $Re_0 = 16330$. A recirculation zone in the vicinity of the jet discharge and the expansion of the jet in the x direction are evident from the data. The corresponding turbulent kinetic energy and total (viscous plus turbulent) streamwise shear stress distributions are show in Figs. 3 and 4, respectively.

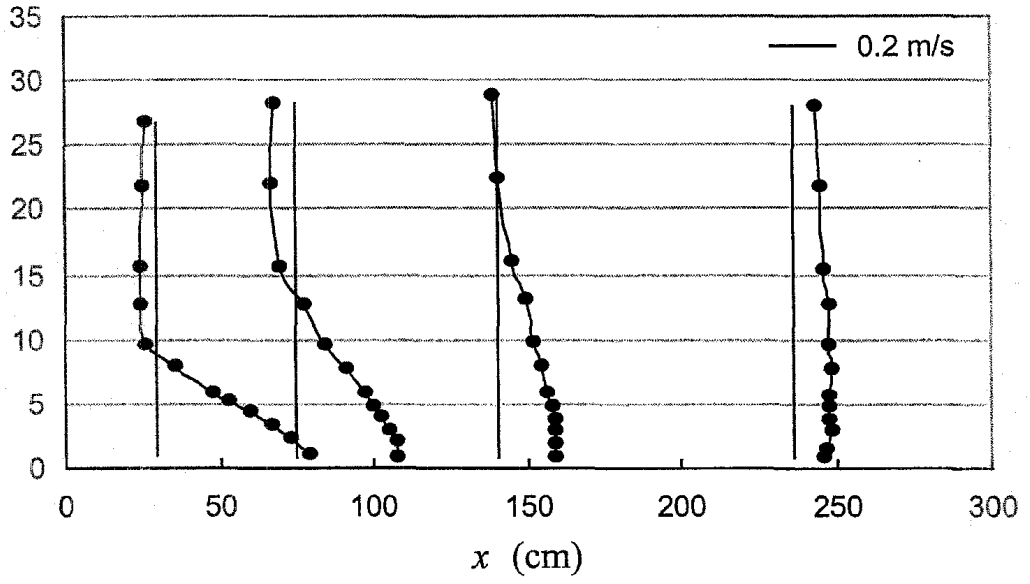

Fig. 2 Variation of flow velocity profile along the centerline of the channel.

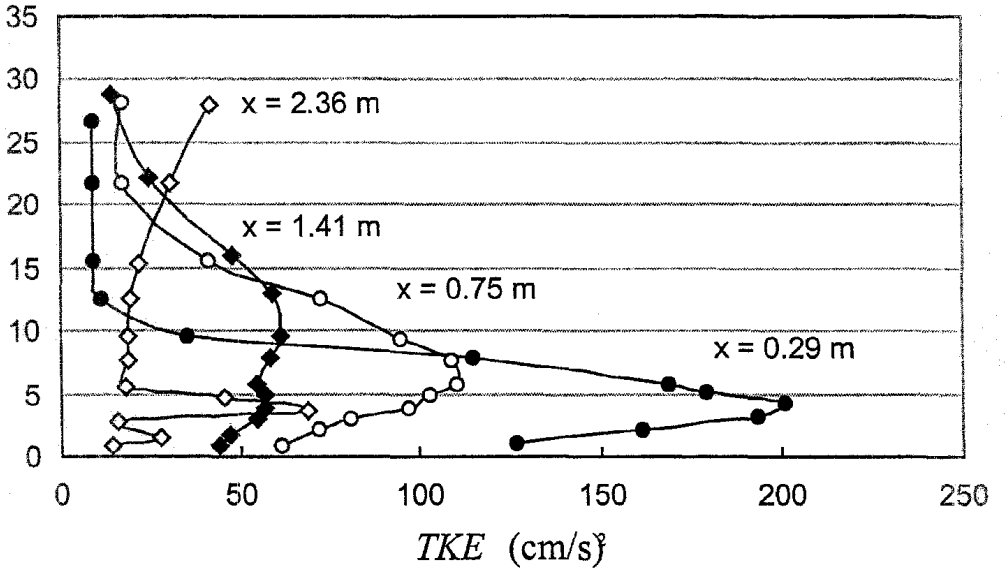

Fig. 3 Variation of vertical profile of turbulent kinetic energy, *TKE*, along the centerline of the channel.

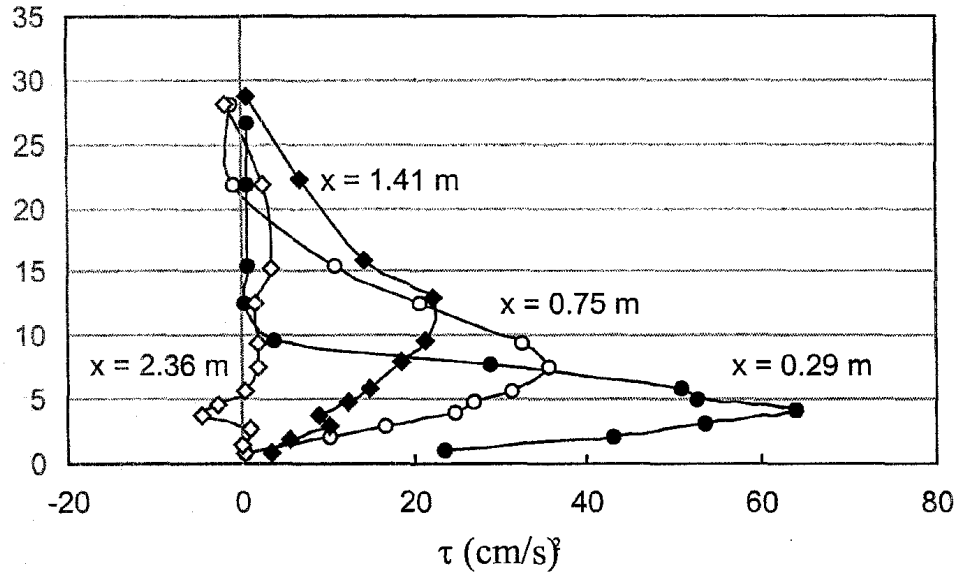

Fig. 4 Variation of vertical profile of total streamwise shear stress, τ, along the centerline of the channel.

Following the procedure outlined in Appendix A, Fig. 5 shows the estimated values of the bed shear stress exerted by the jet, using the rate of change of streamwise momentum along the channel obtained from the velocity information of Fig. 2. A power law was fit to the data and a decay of the bed shear stress with $x^{-1.4}$ is obtained.

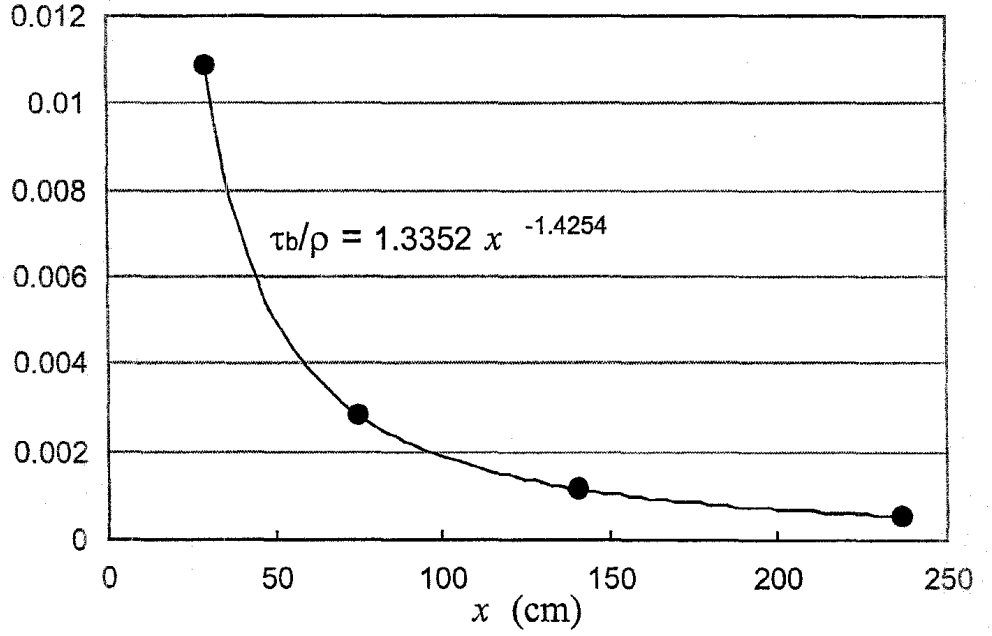

Fig. 5 Variation of bed shear stress along the centerline of the channel.

Erosion in the near field of plane wall jet

The scour generated by a plane wall jet similar to that characterized in Figs. 2 to 5 is illustrated through the sequence of video images of the process shown in Fig. 6. It can be seen in those images that the sediment bed is eroded by the wall jet, such that a front that moves in the streamwise direction is created, that separates the completely scoured bed from the sediment bed downstream.

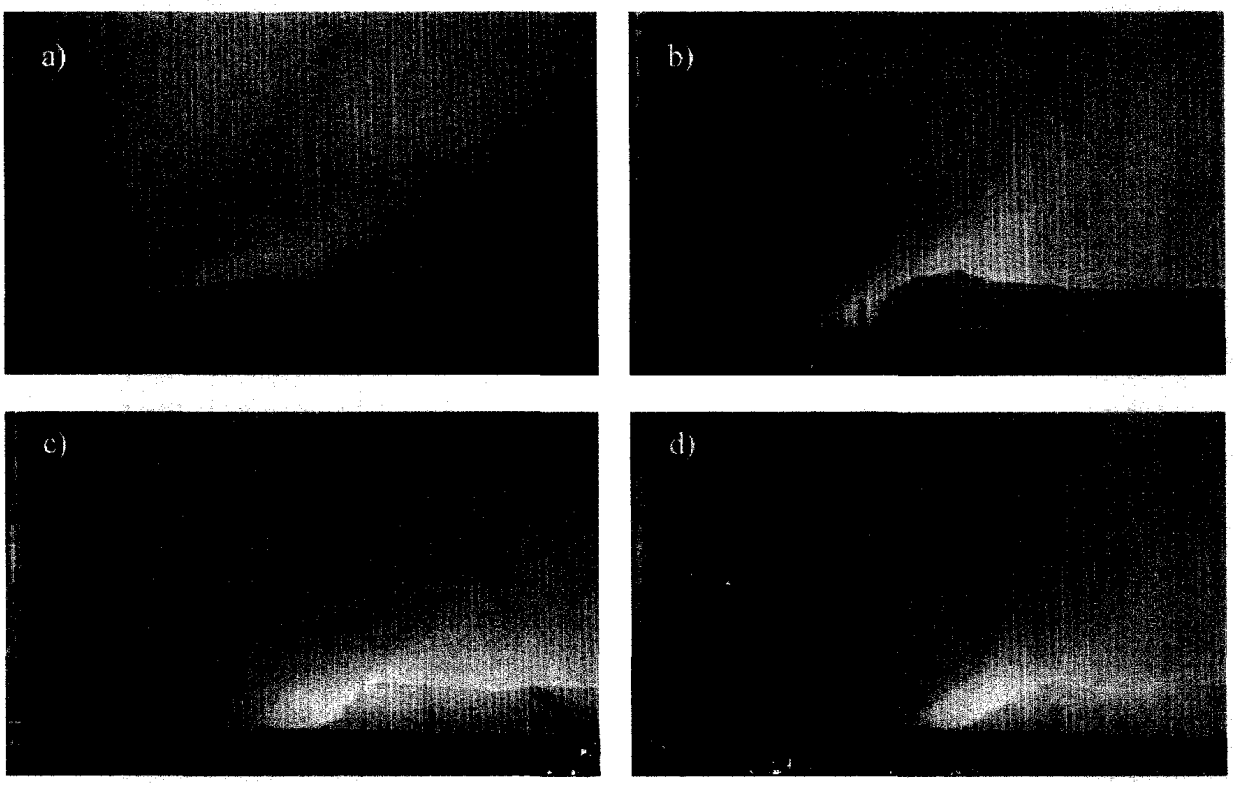

Fig. 6 Sequence of images of the bed erosion process generated by a wall jet. Image a) corresponds to a time $t = 15$ min after initiated the experiment; b) $t = 25$ min; c) $t = 40$ min; d) $t = 55$ min.

The image information obtained can be used to track the position of the front in time, and from that to obtain the erosion rate generated by the wall jet. The results obtained from this analysis for the experiment shown in Fig. 6 are presented in Fig. 7, where the front position and the erosion rate are plotted as a function of time. The erosion rate, or velocity of the scour front, decreases as the front moves away from the jet discharge, as the flow velocity and bed shear stress decay away from the source of momentum. It is interesting to note, as it can be observed in Fig. 6, that the angle of the front with respect to the bottom alternates between almost 90° to about 45°, and this defines a stepwise advancement of the tip of the front. Starting from a vertical front, the bed is eroded with the tip of the front more or less fixed, until a front angle of about 45° is obtained. After that, the tip is rapidly eroded, thus advancing downstream, until the front is again vertical and the procedure repeats all over again. The effect of this erosion mechanism is detected in Fig. 7, as the front location in that figure corresponds to that of the tip. This explains the observed intermittent variation of the front velocity particularly during the first 10 to 15 minutes of the experiment.

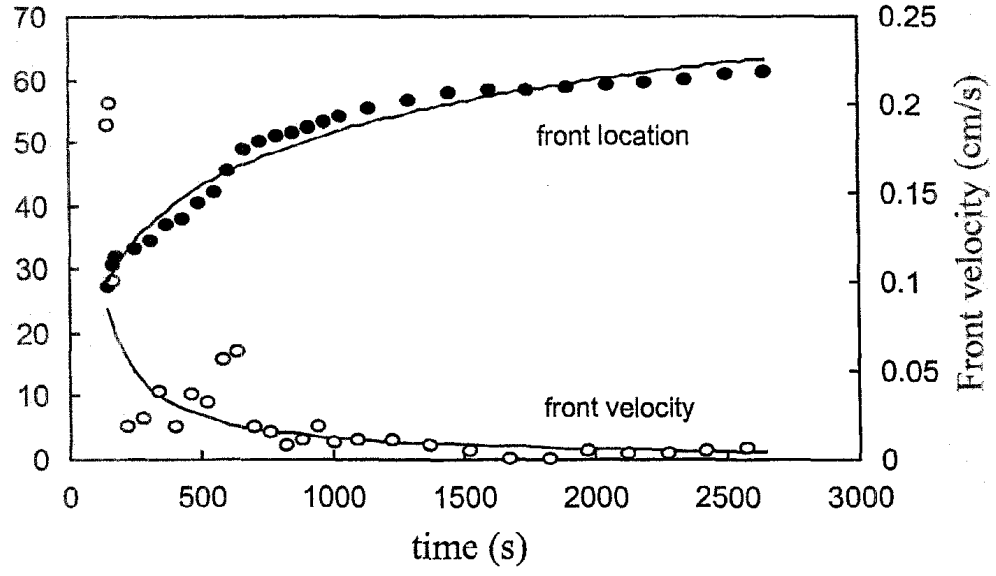

Fig. 7 Location and velocity of the scour front as a funtion of time.

In the present experiments, the eroded sediment was transported downstream mostly in suspension. As the momentum input by the jet discharge is completely dissipated by friction, the only transport mechanism available at the end of the near field region is buoyancy, which drives a turbidity current that is able to transport the entrained sediment to the downstream end of the channel. In the channel reach of about 5 m long, no deposition of the suspended sediment transported by the turbidity current was detected, although no erosion occurred either. This behavior is promising as it validates the main design premise of the jetting system for the management of solids in McCook reservoir: the far field transport capacity of the flow must be large enough as to carry the sediment entrained by the jets away from the reservoir to the drainage channel.